Journal of Energy Storage 109 (2025) 115127

Contents lists available at ScienceDirect

Journal of Energy Storage

journal homepage: www.elsevier.com/locate/est

Research papers

Thermal performance assessment and optimization simulation of large-scale molten salt storage tanks and foundation

Xue Xue, Huaan Li, Cunxian Chen, Fengyongkang Wu, Kelang Jin, Mengting Ji, Hao Zhou *

Zhejiang University, Institute for Thermal Power Engineering, State Key Laboratory of Clean Energy Utilization, Hangzhou 310027, PR China

ARTICLE INFO

Keywords:
Large-scale molten salt storage tank
Temperature field simulation
Heat loss calculation
Foundation bedding

ABSTRACT

This study uses ANSYS to model large-scale molten salt storage tanks and their foundation for concentrated solar power plants, investigating their thermal performance under various conditions. The impacts of factors like ambient temperature, insulation thickness, expanded clay aggregate thickness, and ventilation systems on temperature distribution and heat loss are analyzed. Results show that the heat losses for the hot and cold tanks are 266.89 kW and 206.40 kW, with temperature drops of 0.79 °C and 0.63 °C after 24 h. A decrease in ambient temperature increases cold tank heat loss by 32.58 %, making it more sensitive to temperature changes. While increasing insulation thickness reduces heat flux, the benefits diminish beyond optimal thicknesses of 300 mm for the cold tank and 550 mm for the hot tank. Expanded clay aggregate effectively reduces heat transfer through the foundation, with thickness changes significantly affecting temperature fluctuations. The spacing of ventilation ducts also plays a crucial role in heat dissipation, and optimizing airflow and spacing improves foundation thermal control. This study provides valuable insights for optimizing the thermal performance of molten salt storage tanks, advancing energy storage system design and application.

1. Introduction

The global energy crisis has become a significant factor constraining global development. The transition to renewable energy has emerged as a cornerstone in supporting the world's path towards sustainable development. In 2022, global investments in technological advancements for energy transition reached 1.3 trillion USD, with 500 billion USD allocated specifically to renewable energy. >43 % of the total investment in renewable energy was directed towards utilizing solar energy resources [1]. Compared to photovoltaic solar power plants, one of the primary advantages of concentrated solar power (CSP) plants is that they can be equipped with molten salt thermal storage (MSTS) systems. This allows for heat storage and the capability to generate electricity even after sunset, ensuring a stable supply of solar energy and providing the grid with a continuous source of clean energy [2].

As the market matures, CSP with low-cost thermal energy storage (TES) can potentially integrate a higher share of variable solar energy. This implies that although CSP is often underestimated, it could play a more significant role in the future. By 2050, CSP will account for 11.3 % of global electricity generation [3]. By the end of 2023, the global installed capacity of CSP exceeded 6.5 GW. Since 2018, CSP plants in China have undergone rapid development, with a total installed capacity of 4951.4 MW, and by 2021, the electricity generation exceeded 20 GWh. The successful deployment of CSP has accelerated renewable energy development, yet coal-fired power plants remain the energy mainstay in many regions [4]. Unlike thermal energy, electrical energy is a high-grade form, which has spurred recent advancements in grid energy storage applications for TES. Molten salt-based TES systems, known for their low cost and high scalability, have become a key solution for grid energy storage [5] and flexibility improvements in coal-fired power retrofits [6]. However, most research has centered on innovations in grid storage methods, integration of coal-fired units with TES systems [7] and on improving heat exchange efficiency to enhance operational flexibility [8], while overlooking the inherent safety issues associated with MSTS systems.

A variety of TES systems are available for both CSP plants and power generation system retrofits, each with distinct advantages and limitations [9,10]. Solid particle [11] and phase-change material [12] storage systems offer high energy density and excellent high-temperature resistance but face technical challenges in heat transfer efficiency and temperature control. Oil-salt hybrid systems [13] lack stability at high temperatures and are prone to thermal decomposition. Thermochemical energy storage [14] has high material costs and is not in established

---

* Corresponding author.
E-mail address: zhouhao@zju.edu.cn (H. Zhou).

https://doi.org/10.1016/j.est.2024.115127
Received 11 September 2024; Received in revised form 29 November 2024; Accepted 21 December 2024

Nomenclature

Roman symbols

A	area(m^2)
C_p	constant-pressure specific heat J/(kg·°C)
g	gravitational acceleration(m/s^2)
k	thermal conductivity(W/(m·K))
p	pressure(pa)
q	heat flux(W/m^2)
$\dot{q}$	volumetric heat source
Q_{total}	total heat loss (kW)
T	temperature (°C)
∇T	temperature gradient vector
$\nabla(\rho \vec{u})$	mass flux rate of the fluid
$\vec{u}$	fluid velocity vector

Greek symbols

α	thermal diffusivity (m^2/s)
λ	thermal conductivity (W/(m·°C))
μ	dynamic viscosity (Pa·s)
ρ	density (kg/m^3)

Abbreviation

CSP	concentrated solar power
D-TMS	double-tank molten salt
ECA	expanded clay aggregate
FGB	fine gravel bedding
FSB	fine sand bedding
GB	gravel bedding
MS	molten salt
MSTS	molten salt thermal storage
MSST	molten salt storage tank
PW	partition wall
RSTP	ring support steel plate
SRW	steel ring wall
VD	ventilation duct

industrial use. Single-tank thermocline systems [10] rely on temperature stratification to retain heat, but in practice, thermal mixing is difficult to avoid, leading to increased heat loss and reduced storage efficiency. In contrast, the double-tank molten salt system, with separate high-temperature and low-temperature salt storage, provides stable heat transfer and release. This flexibility and reliability make it the most widely used and mature TES solution for CSP plants today [15]. Among the CSP plants currently operating in China, 46.32 % are equipped with TES systems. Of the CSP plants planned for construction, 61.90 % are designed to include two-tank thermal storage systems (Fig. 1). The Solar Two project successfully implemented molten salt (MS) in a tower CSP plant, utilizing it as both the heat transfer and thermal storage medium. Heat is transferred between a cold and hot tank, making it the most mature D-TMS storage system currently in operation [16].

The molten salt storage tanks (MSST) are similar in shape and size to oil storage tanks, consisting of a tank body, insulation materials, a foundation, and internal piping. However, no standardized evaluation criteria exist for MSST. Their construction is primarily guided by American Petroleum Institute (API) 650 standard [17], the primary reference. Although the API 650 standard provides guidance for the design and construction of storage tanks, it primarily addresses conventional petroleum tanks and does not adequately consider the specific requirements of molten salt storage tanks under high temperatures, thermal cycling, and transient conditions. Therefore, further standards and regulations are needed in the design and evaluation processes of molten salt storage tanks. Although the double-tank molten salt thermal storage system performs excellently in providing stable heat storage and supply, it still faces challenges such as heat loss [18–20], thermal deformation [21], structural fatigue [22,23], foundation settlement [24], and material corrosion [25]. These issues and challenges therefore require further research and identification.

Due to the wide sensible heat usage range of MSST, with operating temperatures typically between 130 °C and 565 °C [26], which is significantly higher than the temperature range of conventional energy storage facilities, there are stringent requirements for tank materials, thermal insulation, heat exchange, and structural strength. The complex temperature distribution and thermal stress issues inside the tank, particularly when the tank wall temperature is uneven, can accumulate thermal stress and structural damage. This can affect the system's long-term operational safety and performance stability. For example, in the 19.9 MW Gemasolar tower CSP plant in Spain [27,28], the MSST have experienced several incidents of cracking and leakage due to thermal stress and uneven foundation settlement. Wan et al. [26] proposed a comprehensive thermal performance evaluation model for MSST to assess heat loss and temperature distribution. The total stress variation over the course of a day is approximately 100 MPa, which could potentially lead to fatigue issues in the tank shell. Additionally, they analyzed the impact of mechanical stress on the foundation structure due to variations in the MSST inventory within the tank, and recommended that the stiffness of the tank filling material for the tank

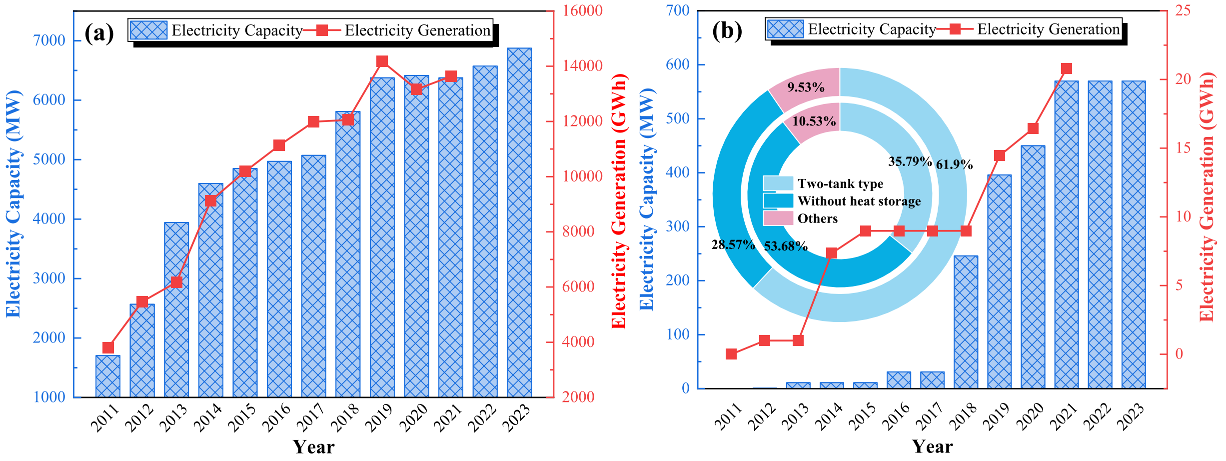

Fig. 1. (a)Global installed capacity and electricity generation of CSP and (b)The status of thermal energy storage systems in CSP plants in China [1].

foundation should be higher than 5 MPa/m. Rodríguez et al. [29] decomposed the storage tank system into different components and applied varying levels of modeling detail to each component. Using the transient thermal simulation of the MSST at the Andasol power plant as an example, they employed a coupled composite wall model to solve the fluid dynamics. Additionally, they found that the vertical wall of the tank rapidly develops a turbulent boundary layer at the start of cooling, and once reaching a quasi-steady state, heat is exchanged at an almost constant rate. Suárez [30] constructed a computational fluid dynamics model to analyze the cooling process of the storage tank during standby periods and investigated the effect of charging levels on heat loss. The study found that standby periods of <3 days do not lead to the freezing of the MSST. The solidification times for the hot and cold tanks are 3–5 days and 8–13 days, respectively. However, the start time of solidification is significantly influenced by the fill level. Peiró et al. [31] conducted charging and discharging experiments at the D-TMS storage test facility at the University of Lleida (Spain). The experiments demonstrated that the optimal arrangement involves opposing flow directions when maintaining a temperature differential of 65 °C across the MSST and the thermal fluid. Additionally, they analyzed the temperature distribution within the tank by installing temperature sensors inside and within the insulation layer. They found that the thickness of the insulation layer and different electrical resistances are the primary factors affecting the tank temperature. Prieto et al. [32] analyzed the MSST pilot plant at Abengoa, where they combined an 8.1 MWh indirect D-TMS system with a parabolic solar field. They calculated and analyzed material corrosion, potential leakage points, storage performance, and actual efficiency of the storage tanks during operation. They found that the tanks experienced significant heat losses and required salt circulation during operation.

The issue of heat loss in MSTS tanks is also a current research focus. Heat loss directly affects the system's energy efficiency and economic viability. Therefore, it is crucial to accurately assess and effectively manage it to minimize energy resource wastage and increase operational costs. Several studies have calculated heat losses for operational D-TMS systems. Radosevich et al. [20] calculated the heat losses for the thermal storage tanks at the CESA-I central receiver plant in Spain, finding a maximum value of approximately 20 kW at a design temperature of 304 °C. Castro et al. [19] estimated that the maximum heat loss for the cold tank at 220 °C is 10 kW. Additionally, Andújar et al. [18] calculated the net thermal-to-thermal efficiency of the thermal storage system to be 72 %, with heat loss coefficients for the hot and cold tanks of 0.327 and 0.265 W/(m^2·K), respectively. Relloso et al. [33] conducted experiments with MSTS in commercial parabolic trough power plants and revealed that, at the highest and lowest salt levels, the daily heat losses for the hot and cold tanks were approximately 1 °C and 5–6 °C, respectively. Schulte-Fischedick et al. [34] performed three-dimensional and two-dimensional modeling of an 880 MWh D-TMS storage system in Spain and calculated the heat loss from the storage tank using the finite element method. The results of the study showed that the heat losses in the side walls and bottom of the storage tank were significant. In an empty tank state, localized solidification of the MSST begins after 3.25 days. Zaversky et al. [35] developed a transient heat loss model for MSTS tanks, accurately describing the governing heat transfer mechanisms. They found that the coefficient of convective heat transfer at the tank bottom, at 565 °C, was 39.8 W/(m^2·K). The modeling process excluded the foundation from the analysis. It was assumed that the temperature of the insulation layer at the tank bottom foundation was constant at 90 °C. Traditionally, heat loss calculations have primarily focused on evaluating the location and amount of heat loss, often overlooking the impact of foundation materials on the tank's heat loss and the temperature field of the foundation. Peiró et al. [31], through experiments at a pilot plant, found that heat losses at the bottom and the cap of the tank (due to direct exposure to air) were higher than those at the middle. The wall surface heat loss was approximately 80 W/m^2, the cap of the tank was 73 W/m^2, and the concrete at the bottom was 61 W/m^2. Stopping the tank's heating system would reduce heat losses at various locations, except for the insulation layer. Prieto et al. [36] calculated the heat losses of an 8.1 MWhth MSST pilot plant built in Spain during a 48-h operational period. Thermographic measurements revealed that most thermal bridges occur at duct joints with different diameters, at the connections of insulation layers, at instrument installations, or other bends and turning points. They suggested that adding insulation to the tank foundation could be effective in reducing heat loss. Zhou et al. [37] established a 1 MWh pilot CSP plant and experimentally determined the temperature distribution and heat loss of the storage tank. When the liquid level dropped from 2040 mm to 1039 mm, the differential temperature of MSST during cooling ranged from 22.1 °C to 41.5 °C, but the overall heat loss changed by only 4.3 %. They also optimized the foundation dimensions through Fluent simulations, finding that widening the insulation material by 500 mm reduced the foundation heat loss by 39.8 % [38].

Currently, most studies on storage tanks operate at temperatures below 200 °C, and the foundations typically consist of a single layer of insulation, with most simulations neglecting the detailed modeling of tank walls and matting. However, high-temperature tanks used in CSP applications operate at temperatures exceeding 550 °C, making heat loss a more significant issue. The innovation of this study lies in the utilization of ANSYS 2022R2 for full-scale modeling of large molten salt storage tanks, providing an in-depth analysis of their dynamic thermal behavior. This research not only considers the complex structure of the foundation bedding but also enables real-time monitoring of the temperature fields and heat losses of the tank under various operating conditions. Furthermore, the study integrates multiple factors such as ambient temperature, insulation thickness, expanded clay aggregate thickness, and ventilation systems to comprehensively analyze their interactions and impacts on the thermal performance of the tank. These innovations provide important theoretical support and practical guidance for enhancing thermal management efficiency and optimizing the design of high-temperature storage tanks.

2. Molten salt storage tanks and foundations

2.1. Structures and models

The model constructed in this study is based on a D-TMS system from a thermal energy storage CSP project with a capacity of 1 million kilowatts located in the northwest region of China. As shown in Fig. 2 (taking the hot tank as an example), the design of the high-temperature MSST follows the API 650 standard [17]. The total height of the tank is 18.146 m, the middle diameter is 32.55 m, and the height of the tank side wall is 14.5 m. The above-ground portion of the storage tank mainly consists of the tank body and the insulation layer. The underground portion of the storage tank serves as a load-bearing and insulating foundation layer, which includes fine sand bedding(FSB), fine gravel bedding(FGB), ring support steel plate(RSTP), steel ring wall(SRW), expanded clay aggregate(ECA), heat-resistant concrete, partition wall (PW), and soil. The specific locations and dimensions can be seen in the schematic diagram at the bottom of Fig. 2. Notably, expanded clay aggregate is used as the primary foundation material to maintain excellent thermal insulation performance. However, due to the generally lower compressive strength of expanded clay aggregate, a heat-resistant concrete partition wall is used to support the expanded clay aggregate. The detailed arrangement between the two can be seen in the schematic diagram in the upper right corner of Fig. 2. Additionally, within the gravel bedding above the bearing layer, 42 ventilation ducts (VD) are arranged in parallel and horizontally. These ducts are spaced with air inlets and outlets on both sides and are designed to dissipate heat from the foundation cushion. Heat is removed from the cushion layer through natural convection or mechanical ventilation, thereby lowering the temperature of the cushion to keep it within a safe range.

All the above components were used to establish the heat transfer

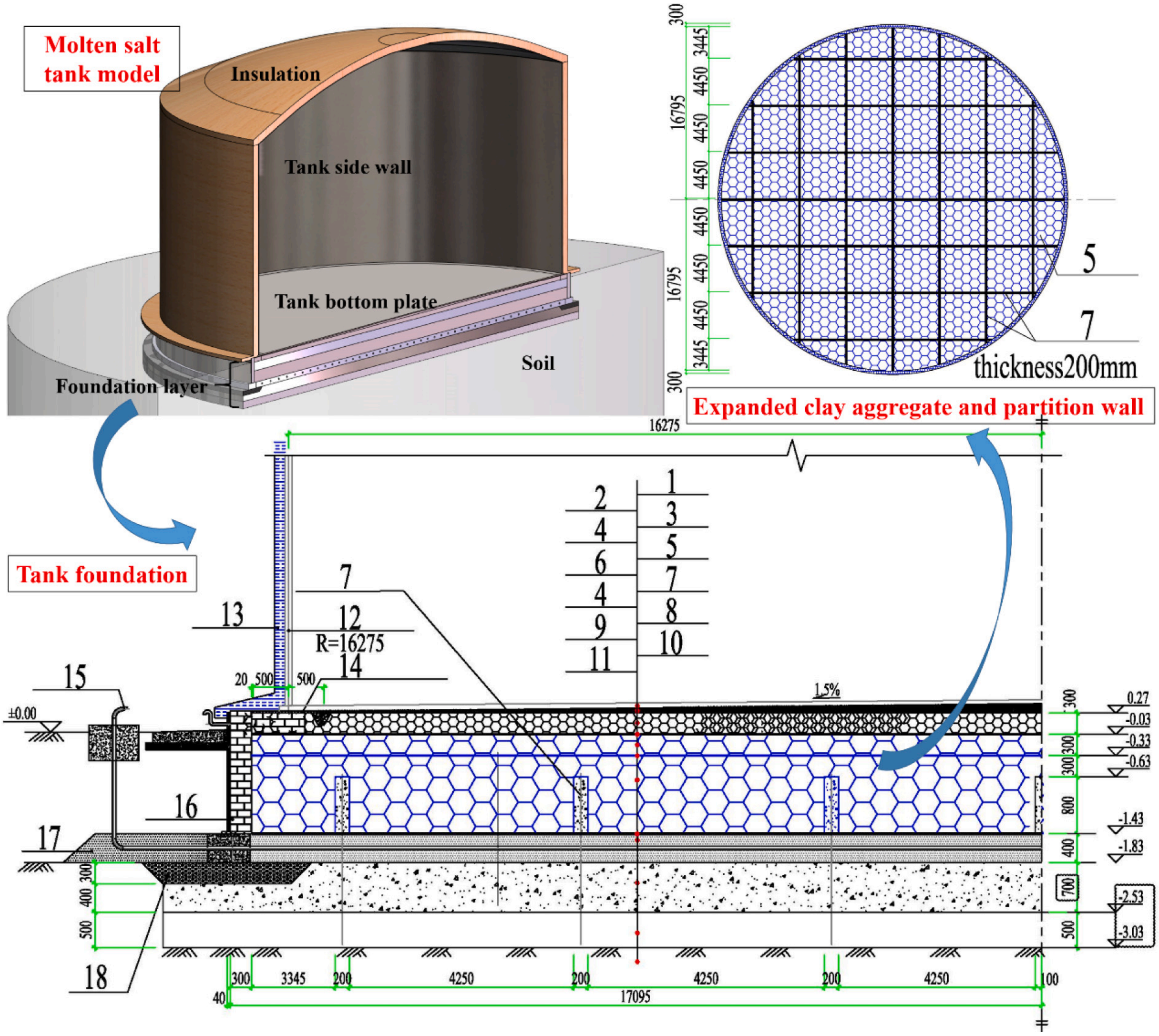

1	Tank bottom plate	2	Fine sand bedding	3	Fine gravel bedding
4	Ceramic fiber cloth	5	Expanded clay aggregate	6	Wire mesh
7	Partition wall	8	Gravel bedding	9	Concrete rigid layer
10	Concrete replacement layer	11	Bearing layer	12	Side wall
13	Insulation layer	14	Ring support steel plate	15	Ventilating pipe
16	Firebrick	17	Fine gravel	18	Coarse gravel

Fig. 2. Molten salt tank and foundation structure.

analysis model for the hot and cold tanks. The computational domain of the model includes the fluid domain (MS and air) and the solid domain (tank body, foundation cushion, etc.). Due to the need for complex charging and discharging operations as well as special working conditions in high-temperature MSST, a significant number of nozzles and ducts are arranged inside the tank. However, the primary objective of this study is to evaluate the heat loss and temperature distribution within the tank. Therefore, structures with minimal impact on temperature and strength were simplified, while those with significant effects were retained in the model.

2.2. Materials and properties

The D-TMS system contains high-temperature MS within the tanks. Therefore, to meet the requirements for high-temperature resistance and corrosion prevention, the hot tank material selection is A516 *Gr.*70 and the cold tank material selection is A240 Type 347H. Based on the insulation requirements, aluminum silicate is chosen as the insulation material, with the insulation thickness set at 300 mm for the hot tank and 550 mm for the cold tank.

At present, there is no specific standard document for the design of molten salt storage tanks, usually referring to the design standards for oil storage tanks and other relevant documents. The main reference design specification in this project is from API 650 [17]. In addition, the parameters of insulation materials, tank steel, foundation bedding materials, etc. are also referred to the Chinese national standard documents [39–42]. As shown in Table 1, the material parameters of the double-tank thermal storage system are presented. The heat loss generated by the tank body and MS during operation leads to temperature variations, which in turn affect thermal performance. To accurately reflect the

Table 1
Material properties of double-tank heat storage systems.

(a) Foundation material [40,42]

Material layer	Thermal conductivity (W/m·°C)	Elasticity's modulus (×10^3 MPa)	Poisson's ratio	Expansion coefficient (×10^{-6}/°C)	Density (kg/m^3)
Insulation	0.08	–	–	–	480
Fine sand bedding	1.10	0.02	0.30	7.00	2500
Fine gravel bedding	2.50	0.09	0.30	7.00	2500
Gravel bedding	2.00	0.09	0.30	7.00	2500
Firebrick	0.12	0.01	0.30	5.50	2000
Steel ring wall	58.00	210.00 (20 °C) 154.00 (570 °C)	0.20	0.12	7850
Concrete	1.10	25.50	0.20	0.10	2500
expanded clay aggregate	0.11–0.34	2.00	0.32	7.00	3500
Soil	1.50	0.22	0.38	0.10	2000

(b) Tank body [39,41]

Metal material	T(°C)	Thermal conductivity (W/(m·°C))	Elasticity's modulus (×10^3 MPa)	Poisson's ratio	Expansion coefficient (10^{-6} mm/mm/°C)	Density (kg/m^3)
A240 Type347H	100.00	15.40	189.00	0.31	16.20	8030.00
	150.00	16.10	186.00	0.31	16.60	8030.00
	200.00	16.80	183.00	0.31	17.00	8030.00
	250.00	17.60	179.00	0.31	17.40	8030.00
	300.00	18.30	176.00	0.31	17.70	8030.00
	350.00	19.00	172.00	0.31	7.90	8030.00
	400.00	19.70	169.00	0.31	18.10	8030.00
	450.00	20.50	165.00	0.31	18.30	8030.00
	500.00	21.20	160.00	0.31	18.40	8030.00
	550.00	21.90	156.00	0.31	18.60	8030.00
	600.00	22.60	151.00	0.31	18.80	8030.00
A516 *Gr.*70	100.00	58.00	198.00	0.30	12.10	7750.00
	150.00	55.90	195.00	0.30	12.40	7750.00
	200.00	53.60	192.00	0.30	12.70	7750.00
	250.00	51.40	189.00	0.30	13.00	7750.00
	300.00	49.20	185.00	0.30	13.30	7750.00
	350.00	47.00	179.00	0.30	13.60	7750.00
	400.00	44.90	171.00	0.30	13.80	7750.00
	450.00	42.70	162.00	0.30	14.10	7750.00
	500.00	40.50	151.00	0.30	14.40	7750.00

(c) Molten salts [43]

Parameter	Formulas	Value ($T = 290$ °C)	Unit
Specific heat (C_p)	$1443 + 0.172 \times T$	1493	J/(kg·°C)
Thermal conductivity (λ)	$0.4433 + 0.19 \times 10^{-4} \times T$	0.4984	W/(m·°C)
Thermal diffusivity (α)	$1.410 \times 10^{-7} + 1.157 \times 10^{-10}\, T$	1.75×10^{-7}	m^2/s
Dynamic viscosity (μ)	$(22.714–0.120 \times T + 2.281 \times 10^{-4} \times T^2–1.474 \times 10^{-7} \times T^3) \times 10^{-3}$	0.0035	Pa·s
Density (ρ)	$2090–0.636 \times T$	1906	kg/m^3

temperature and thermal performance of the heat storage tank system, the thermal properties at different temperatures or corresponding formulas are input into the computational model. The maximum MS level in the hot tank is 13.3 m, while in the cold tank it is 13.2 m. A 19,000 t binary salt mixture, consisting of 60 wt% $NaNO_3$ and 40 wt% KNO_3, is selected as the thermal storage medium, which is sufficient to meet the 8 h storage duration for a 100 MW thermal storage system.

3. Numerical methods and boundary conditions

3.1. Thermal analysis

The mechanism of heat transfer in the MSST system is a complex and multi-layered process that encompasses three fundamental modes of heat transfer: conduction, convection, and radiation. As illustrated in Fig. 3, these modes interact with each other, collectively determining the system's thermal transfer efficiency and stability. Firstly, the MS within the tank acts as a heat source. For the tank side wall not submerged in MS, convection and radiation are the main heat transfer methods between the MS and the side wall of the tank. Convection involves the movement of air, which transfers heat from the surface of the MS to the air, and then the heat is conveyed to the tank side wall and insulation layers, further dispersing and distributing the thermal energy. Heat is transferred through conduction and convection for the tank side wall that are submerged in MS (including the tank bottom). The insulation material, located on the exterior of the tank side wall, dissipates heat to the outside through natural convection with the surrounding air. The heat absorbed by the tank bottom is continuously transferred to the foundation layers below. Initially, the heat is conducted to the fine sand bedding, followed by the fine gravel bedding, with heat loss occurring at each successive stage. Ultimately, the heat is transferred to the deeper soil. The heat transfer between the foundation layers is primarily conducted through thermal conduction. Additionally, within the gravel bedding(GB), forced convection heat exchange occurs between the ventilation ducts and the surrounding air.

3.2. Governing equations

The following governing equations were selected to describe the thermal analysis process of the MSST and its foundation. Furthermore,

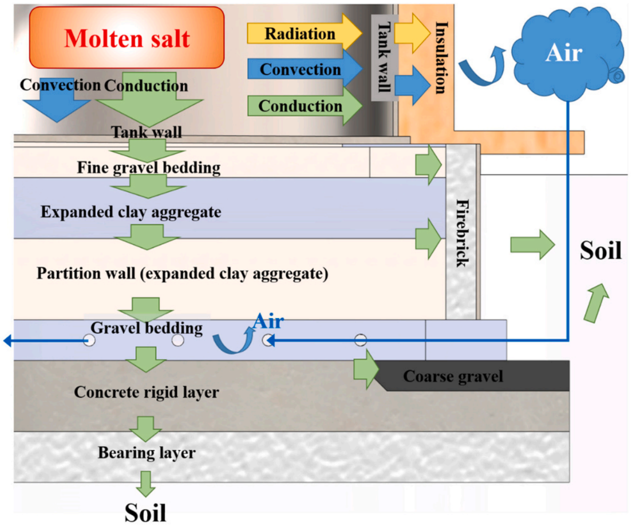

Fig. 3. Heat transfer of the tank.

by comprehensively considering the flow characteristics of the MS, the airflow behavior within the ventilation ducts, and the thermal coupling effects between solids and fluids, detailed numerical simulations have been provided to support the distribution and variation of the temperature field within the system. This approach offers a deep theoretical foundation and practical guidance for optimizing the design of the MSST and its foundation. The equations selected from the ANSYS® Fluent module and the meanings of the symbols in the equations are as follows:

The continuity equation for the simulation is given by Eq. (1):

$$\frac{\partial(\rho u)}{\partial x}+\frac{\partial(\rho v)}{\partial y}+\frac{\partial(\rho w)}{\partial z}=0 \tag{1}$$

The mass conservation equation (Eq. (2)) ensures the continuity of flow for both the MS inside the tank and the air within the ventilation ducts, describing the changes in mass over time and space. In this equation, ρ represents the fluid density, $\overrightarrow{u}$ is the fluid velocity vector, and $\nabla\cdot(\rho\overrightarrow{u})$ denotes the mass flux rate of the fluid.

$$\frac{\partial\rho}{\partial t}+\nabla\cdot(\rho\overrightarrow{u})=0 \tag{2}$$

The momentum equation (Eq. (3)) describes the fluid's internal motion state, including the effects of acceleration, pressure, and gravity. In this equation, p is the pressure, μ is the dynamic viscosity of the fluid, and g is the gravitational acceleration.

$$\rho\left(\frac{\partial\overrightarrow{u}}{\partial t}+u\cdot\nabla\overrightarrow{u}\right) = -\nabla p+\nabla\cdot(\mu\nabla\overrightarrow{u})+\rho\overrightarrow{g} \tag{3}$$

The energy equation (Eq. (4)) describes the processes of internal energy transfer and transformation, including the effects of heat conduction, convection, and volumetric heat sources. In this equation, T is the temperature, C_p is the specific heat capacity, k is the thermal conductivity, and $\dot{q}$ represents the volumetric heat source.

$$\rho c_p\left(\frac{\partial T}{\partial t}+\overrightarrow{u}\cdot\nabla T\right) = \nabla\cdot(k\nabla T)+\dot{q} \tag{4}$$

The energy equation for the outer wall of the tank and the insulation layer is given by Eq. (5) [22,23], where the subscript i represents either the outer wall or the insulation layer.

$$\frac{\partial(\rho_i c_{p,i} T_i)}{\partial t} = \nabla\cdot(k_i\nabla T_i) \tag{5}$$

In the thermal analysis simulation of MSST and their foundations, it is essential to choose appropriate physical models and solution methods to ensure the accuracy and reliability of the results. The Coupled method is used for solving the equations. The Realizable k-ε turbulence model is used to calculate the flow and heat transfer near the tank side wall and within the ventilation ducts [44,45]. The Discrete Ordinates Model (DOM) [46] is employed to account for the effects of thermal radiation. This model is particularly suitable for high-temperature environments where radiative heat transfer is significant. The radiative heat transfer can be represented by Eq. (6). Where, I_ν is the radiative intensity(W/m^2·sr), Ω is the direction of radiation, θ is the angle of radiation, σ_ν is the absorption coefficient (m^{-1}), S_ν is the radiative source term.

$$\frac{d}{d\Omega}(I_\nu \bullet \cos(\theta)) = -\sigma_\nu I_\nu + S_\nu \tag{6}$$

The radiation equation solved by DOM is coupled with the energy equation to ensure that the interactions between radiation, conduction, and convective heat transfer are comprehensively considered within the thermal model. The energy equation, which takes into account the effects of radiation, can be expressed as Eq. (7). where: Q_{conv} is the convective heat source term (W/m^3), Q_{rad} is the radiative heat source term, computed using DOM.

$$\frac{\partial(\rho c_p T)}{\partial t}+\nabla\bullet(\rho c_p T u) = \nabla\bullet(k\nabla T+Q_{conv}+Q_{rad}) \tag{7}$$

Evaluating the heat loss from the storage tank helps to improve the system's thermal energy storage efficiency, reduce heat loss, and lower operating costs. Additionally, monitoring the temperature decrease of the tank and its foundation can predict and prevent potential overheating or cooling issues, ensuring stable operation of the system under various operating conditions.

The heat flux (q) represents the amount of thermal energy passing through a unit area per unit time, measured in W/m^2. It is a crucial indicator for assessing the rate of heat transfer through space. Fourier's law describes the process of heat conduction within a material. For one-dimensional conduction, the Eq. (8) is:

$$q = -k\frac{dT}{dx} \tag{8}$$

where, k represents the thermal conductivity of the material (W/(m·K)). $\frac{dT}{dx}$ is the temperature gradient. The negative sign indicates that heat flows from high-temperature to low-temperature regions. This law can be extended to multidimensional spaces and is represented in vector form as Eq. (9):

$$q = -k\nabla T \tag{9}$$

where, q is the heat flux vector, and ∇T is the temperature gradient vector, representing the rate of temperature change in various directions.

Heat loss calculation is performed using Eq. (10), where i represents different components of the storage tank, Q_{total} denotes the total heat loss (kW), and A represents the area of each component (m^2).

$$\begin{aligned} Q_i &= Aq_i \\ Q_{total} &= \sum\nolimits_{i=1}^{n} Q_i \end{aligned} \tag{10}$$

The temperature drop (ΔT) can be estimated using the heat loss and the heat capacity of the MS, as shown in Eq. (11). In this equation, Δt represents time (s), m denotes the total mass of the MS in the storage tank (kg), and C_p is the specific heat capacity of the MS (J/(kg·K)).

$$\Delta T = \frac{Q_{total}\Delta t}{mC_p} \tag{11}$$

3.3. Boundary conditions

Due to the gradient variation in the thickness of the tank side wall, ranging from 10 mm to 43 mm, with the thinnest point at the tank's cap, the thermal conductivity of the tank side wall material is relatively high, and the thickness has little effect on heat transfer. Therefore, the dimensions of the tank side wall have been averaged. Additionally, the height difference between the outer and middle rings of the tank bottom is neglected. In the MSST, the salt is at its maximum operational liquid level, the height of the hot tanks is 13,300 mm and the height of the cold tanks is 13,200 mm. The MS temperature inside the tank and at the interface is nearly constant [29], so the convective heat transfer between the MS and the tank side wall is neglected. The submerged tank side wall is assumed to be at constant temperatures (565 °C in the hot tank and 290 °C in the cold tank). A gap exists between the tank's external wall and the insulation layer; therefore, radiative heat transfer in this region needs to be considered. The emissivity of the tank's outer wall is set at 0.7, while the emissivity of the insulation layer is 0.9 [47]. The side and cap of the tank use convective heat transfer boundary conditions, with the air temperature set to 50 °C, which is the safety temperature for the insulation layer. The environmental wind speed is 5 m/s. The convective heat transfer coefficient is determined by Eq. (12) [35].

$$Nu = 0.3 + \frac{0.62 Re^{0.5} Pr^{1/3}}{\left(1 + (0.4/Pr)^{2/3}\right)^{1/4}} \left(1 + \left(\frac{Re}{282,000}\right)^{5/8}\right)^{4/5} \tag{12}$$

Ventilation ducts in the tank foundation are used to remove excess heat from inside the tank and its foundation to prevent overheating. The air inlet temperature of the ventilation ducts in the tank foundation is 25 °C. An airflow rate of 2.62 kg/s at the inlet of the hot tank and 2.26 kg/s at the inlet of the cold tank. The outlet of the ventilation duct is set as an open boundary condition. Each of the two neighboring vent ducts has an opposite direction of air flow. The surrounding soil of the tank is set with isothermal boundary conditions, with a temperature of 25 °C, which is the daily ambient temperature.

3.4. Validation of mesh and numerical model

Mesh generation is a crucial step in finite element analysis, directly affecting the accuracy of numerical simulation results and computational efficiency. The Meshing module in ANSYS Workbench was used for mesh generation. Due to the complex geometry and varying wall thickness of MSST, high mesh quality is required. During the mesh generation process, mesh types suitable for the geometric features of the MSST, including tetrahedral and hexahedral elements, were selected. To accurately capture changes in wall thickness and details of internal structures, both automatic and manual mesh generation methods were employed in the Meshing module. Manual adjustments involved local mesh refinement in critical areas (such as welds, the tank side wall, the insulation layer, and the ring support steel plate) to enhance computational accuracy and obtain precise temperature and heat loss values. Among these, the insulation layer has 6 mesh layers, the tank side wall has 2 mesh layers, and the ring support steel plate has 2 mesh layers. A mesh independence verification was performed to save computational resources and obtain accurate results. We selected the minimum temperature at the cap of the hot tank and the maximum temperature at the lowest layer of the base (bearing layer) under baseline conditions as verification standards. The verification results are shown in Fig. 4. The meshes with 6,979,273 and 6,274,079 elements met the computational requirements.

Heat loss tests carried out in April 1997 in the Solar II project [48] showed that the heat loss in the hot and cold water tanks was about 102 kW and 44 kW respectively. Simulations using the model developed in this research yielded thermal losses of 117 kW and 50.16 kW, respectively. The acceptable deviation in thermal loss calculations is attributed to inconsistencies in boundary conditions and the effects of the tank foundation cooling structure. Additionally, to more accurately validate the correctness of the model, computational analyses were conducted on the different tank models, as shown in Fig. 5. To save computational resources, Rodríguez et al. [29] employed a parallel modular object-oriented methodology that segmented different tank components into independent models for coupled calculations. Their analysis showed a total thermal loss of 194 kW when the tank was fully loaded. In this study, geometric details of the tank wall were standardized due to meshing limitations, with wall thickness increased at higher levels. This led to an underestimation of wall and bottom thermal losses, with an error within 4 kW. As depicted in Fig. 5(b), Wan et al. [26] used the ANSYS® Fluent module to perform two-dimensional steady-state calculations for a tank with a thermal storage capacity of 110 MWh, finding thermal losses in the hot and cold tanks were underestimated by 13.5 kW and 8.4 kW, respectively. In this study, the error in verifying hot tank thermal loss was 9.6 kW, attributed to the inclusion of base ventilation convective heat transfer, rendering results closer to actual conditions.

The study employed CFD to construct some models of similar dimensions as mentioned above and performed thermal loss calculations for the tank. Specifically, the hot tank in the Solar Two project had an inner diameter and height of 11.6 m and 8.4 m, respectively, while in the study by Rodríguez et al. [29], the hot tank had an inner diameter of 38.5 m and a height of 14 m. These dimensions do not significantly differ from the model size considered in this study. A comparison of thermal loss results reveals average errors of 2.18 % and 3.31 % (Fig. 5), supporting the suitability of the present model for evaluating thermal loss in storage tanks of similar sizes. It also validates the rationality and accuracy of the proposed method for thermal performance analysis of storage tanks.

3.5. Case design

To comprehensively analyze the temperature field, thermal loss, and

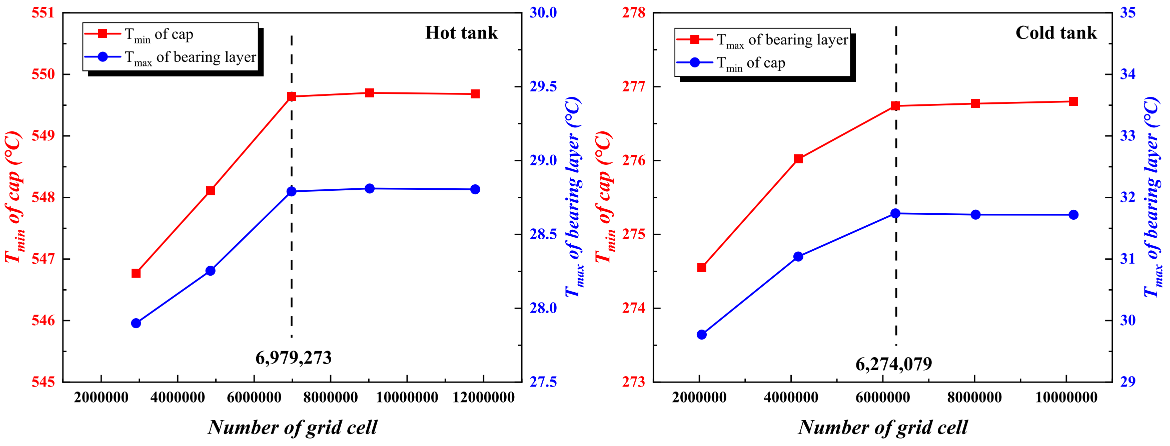

Fig. 4. Grid independence verification.

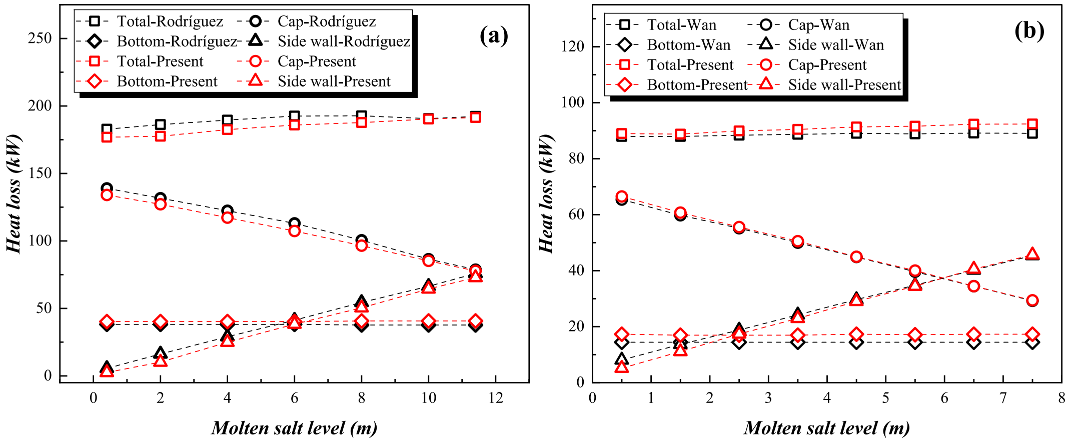

Fig. 5. Validation of thermal analysis models for molten salt tanks.

influencing factors of the storage tanks, both the hot and cold tanks were modeled and analyzed separately in Table 2. Additionally, based on the baseline conditions, the effects of environmental temperature, insulation thickness, expanded clay aggregate thickness, airflow rate through the ventilation ducts, and spacing between the ventilation ducts on the thermal conduction of the tanks, particularly the foundation, were discussed. Here, H1 and C1 represent the first case for the hot and cold tanks, respectively, serving as the base cases for overall thermal performance analysis.

4. Results and discussion

4.1. *Thermal performance evaluation of the base case*

The state of the base case (H1 and C1) was analyzed in depth to evaluate the thermal performance of the MSST system. This process reveals the temperature field distribution and thermal loss of the tank body and foundation layers under standard operating conditions. The temperature distribution maps of the tank body, insulation layer, and foundations can be obtained by conducting detailed temperature field simulations of the base case.

Fig. 6 shows the temperature distribution and fluctuation at different positions of the storage tank, including maximum, minimum and average temperatures. As illustrated in Fig. 6(a), although the temperature ranges for the hot and cold tanks differ, they exhibit similar distribution trends. For instance, in the hot tank, the temperature of the tank body remains relatively high, around 565 °C. Fig. 6(b) highlights notable temperature gradients at specific locations, such as the insulation layer, firebricks, and expanded clay aggregate. The temperature reduction in the fine sand and gravel bedding near the tank bottom is <25 °C, owing to the high thermal conductivity and thinness of these layers, which allow for rapid heat transfer to the lower foundation layers. Expanded clay aggregate, with its low thermal conductivity, primarily serves as insulation; it reduces the temperature by 527.83 °C once the heat reaches it from the tank bottom. Additionally, significant temperature variations are observed in the surrounding annular support materials, with the temperature gradient in the firebricks exceeding 500 °C. This is because all of these materials have one side in direct contact with the high temperature material, for example, the inner layer of the insulation is in direct contact with the tank wall, the upper layer of the refractory bricks will be in direct contact with the ring support steel plate, and the ECA is in close contact with the gravel bedding. These materials, however, have a low thermal conductivity and thus excellent thermal insulation, resulting in extremely low temperatures on the other side.

The insulation layer is crucial for retaining heat within the tank and minimizing heat loss. Fig. 7 summarizes the temperature variation in the vertical direction on the insulation layer's inner and outer sides. The temperature fluctuation on the inner side is minimal, staying within 2 °C. This is due to the tight contact of the insulation layer with the tank side wall, ensuring good thermal contact and reducing discontinuities and local temperature differences in heat transfer. A slight decrease in the MS temperature at higher levels in the tank also results in a 4.42 °C temperature drop in the insulation layer at these heights. This effect similarly causes a temperature reduction on the outer layer at the same locations. The heat transfer process from the tank body to the inner side

Table 2
Simulated design conditions.

Case	Environmental temperature (°C)	Insulation thickness (mm)	expanded clay aggregate thickness (mm)	Ventilation (kg/s)	Ventilation duct spacing (mm)
H1/C1	25/25	550/300	1400/1250	2.62/2.26	730/730
H2/C2	−35/−35	550/300	1400/1250	2.62/2.26	730/730
H3/C3	−5/−5	550/300	1400/1250	2.62/2.26	730/730
H4/C4	55/55	550/300	1400/1250	2.62/2.26	730/730
H5/C5	25/25	400/150	1400/1250	2.62/2.26	730/730
H6/C6	25/25	450/200	1400/1250	2.62/2.26	730/730
H7/C7	25/25	500/250	1400/1250	2.62/2.26	730/730
H8/C8	25/25	600/350	1400/1250	2.62/2.26	730/730
H9/C9	25/25	550/300	800/650	2.62/2.26	730/730
H10/C10	25/25	550/300	1000/850	2.62/2.26	730/730
H11/C11	25/25	550/300	1200/1050	2.62/2.26	730/730
H12/C12	25/25	550/300	1400/1250	0.62/0.26	730/730
H13/C13	25/25	550/300	1400/1250	1.62/1.26	730/730
H14/C14	25/25	550/300	1400/1250	3.62/3.26	730/730
H15/C15	25/25	550/300	1000/850	2.62/2.26	1730/1730
H16/C16	25/25	550/300	1000/850	2.62/2.26	1930/1930
H17/C17	25/25	550/300	1000/850	2.62/2.26	2230/2230

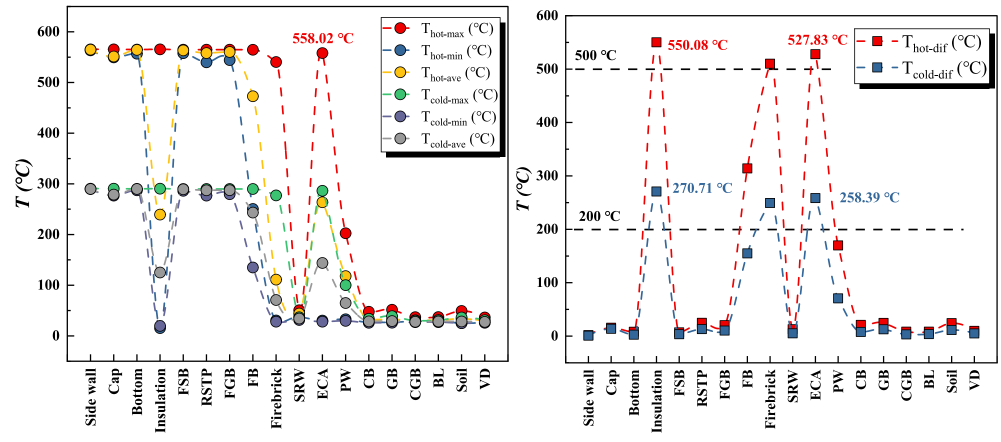

(a) Temperature distribution (b) Temperature fluctuation

Fig. 6. Temperature conditions at different locations of the tank.

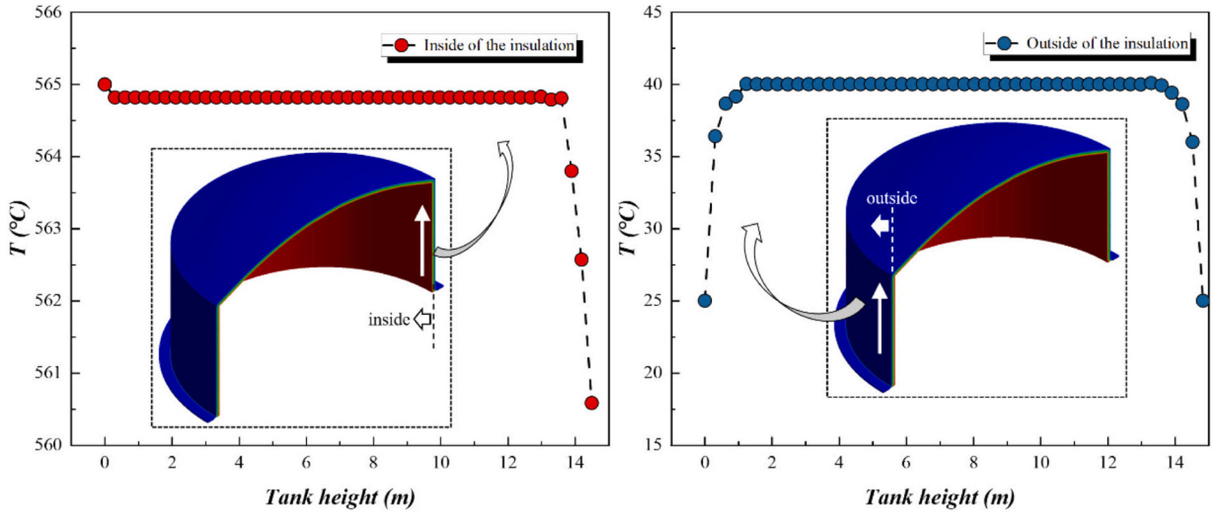

(a) Inside (b) Outside

Fig. 7. Vertical temperature change of insulation.

of the insulation layer gradually diminishes. As observed from the contour plot, the base layer of the outer side of the insulation layer is thicker, leading to a temperature close to the environmental temperature of 25 °C. The excellent insulating properties, appropriate thickness, and uniform thermal transfer characteristics of the insulation layer contribute to maintaining minimal temperature fluctuations on both sides.

The firebricks exhibit significant temperature fluctuations as a crucial supporting ring wall in the foundation material (see Fig. 6(b)). This is due to the firebricks' height exceeding 1700 mm and their contact with various types of underlying layers, spanning multiple temperature ranges in the vertical direction. As shown in Fig. 8(e), the temperature on the inner side decreases from 540.13 °C to 45.91 °C, while the outer side temperature remains stable. The circumferential temperature variation on the upper side of the firebricks is minimal (see Fig. 8(a-b)) because the upper inner layer of the firebricks is in contact with the ring support steel plate, which has good thermal conductivity and is in contact with the tank bottom, maintaining a higher temperature. However, there is a temperature fluctuation of 15.01 °C on the lower side due to its contact with the gravel bedding where the ventilation ducts are located. The spacing of the ventilation ducts causes uneven heat transfer around this area. Similarly, this causes a temperature variation of 2.40–4.77 °C at the external part of firebricks, (see Fig. 8(c-d)). The high-temperature gradient on the upper and lower sides of the firebricks may lead to significant thermal stresses, potentially causing cracks or fissures that could affect the overall structural stability and performance.

The schematic cloud map illustrates the overall temperature distribution of the expanded clay aggregate. The upper surface in contact with the fine gravel bedding shows high temperatures exceeding 550 °C. The low thermal conductivity of the expanded clay aggregate significantly reduces the heat transfer from the tank to the foundation, helping to maintain stable temperatures within the foundation material. This effectively minimizes heat loss and prevents overheating of the foundation, with the lower surface temperature decreasing to below 55 °C. Fig. 9(a) shows the temperature variation along the outer ring of the upper surface, with fluctuations within 3.33 %. Fig. 9(b) describes the lateral temperature distribution of the schematic cloud map through temperature cross-sections of the upper and lower surfaces. The temperature is lower on both sides of the upper surface cross-section, while

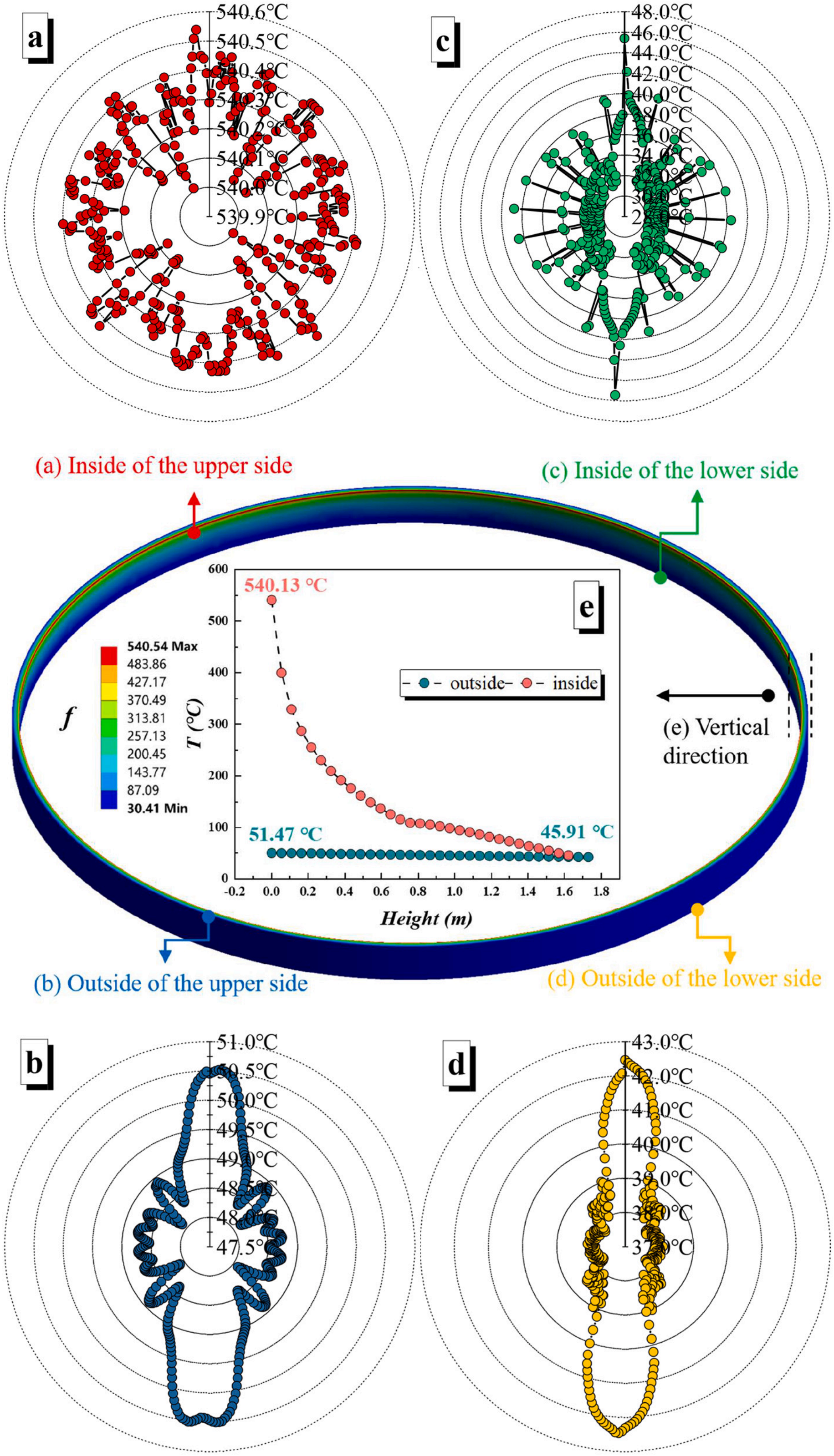

Fig. 8. Temperature distribution of firebrick.

most of the central area maintains a temperature of around 550 °C, as evidenced by the cloud map. The temperature of the lower surface cross-section experiences a 16.78 % fluctuation due to the presence of the partition wall, with the highest temperature at the center reaching 50.71 °C. Additionally, the 494.60 °C temperature difference between the upper and lower surface cross-sections further validates the effective thermal insulation provided by the expanded clay aggregate.

In the foundation layer of the tank, ventilation ducts are installed within the gravel bedding, with spaced air inlets and outlets. As shown in Fig. 10, the temperature distribution in the gravel bedding exhibits

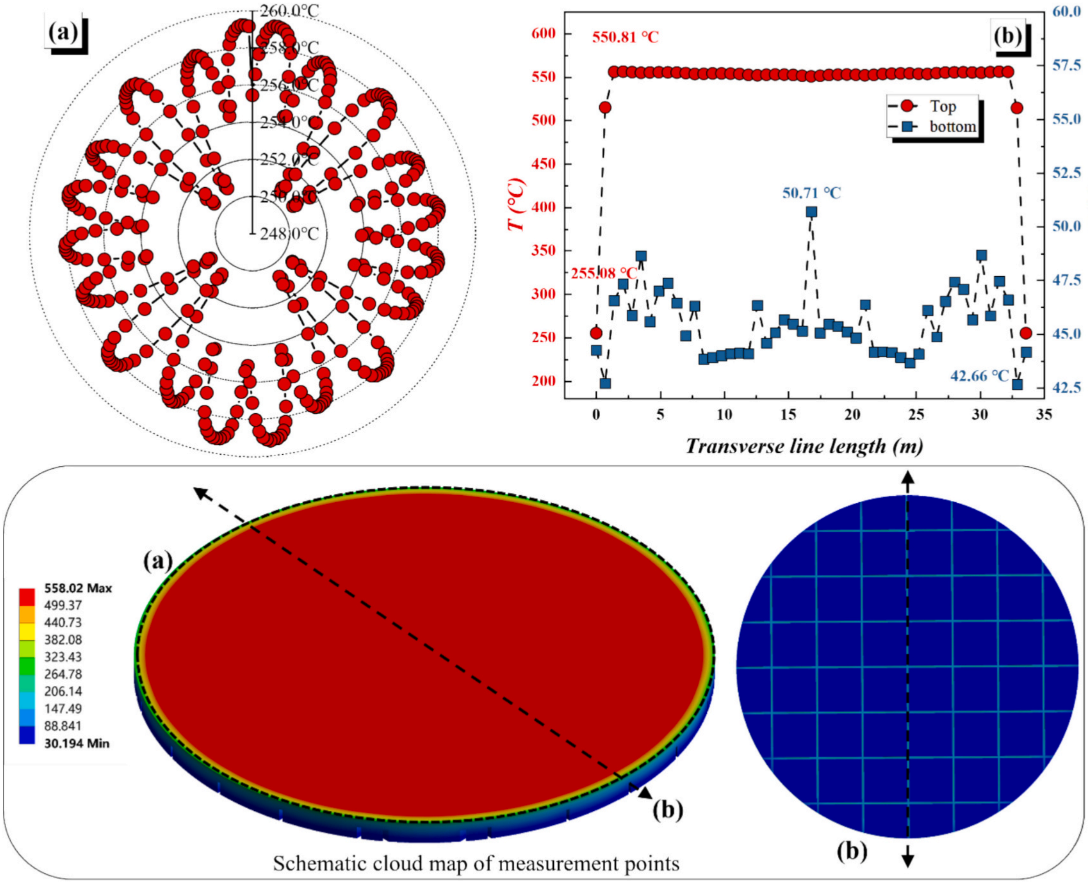

Fig. 9. Temperature distribution of expanded clay aggregate.

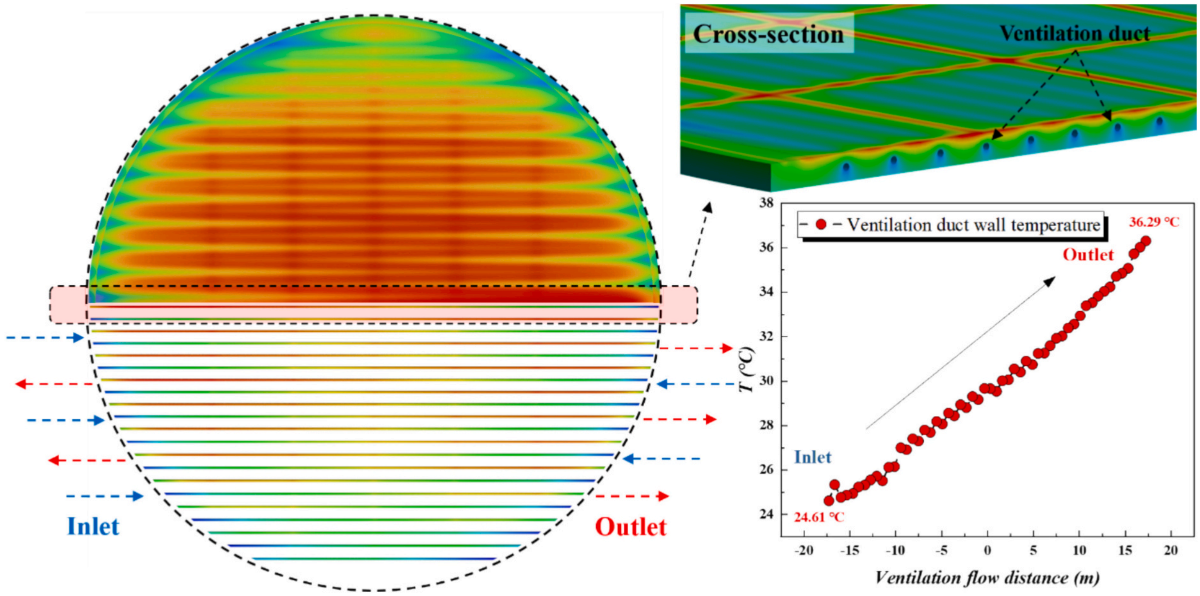

Fig. 10. Temperature distribution of the ventilation ducts.

alternating high and low-temperature regions. The point and line graphs and ventilation ducts cloud map in the lower right corner of Fig. 10 illustrate the linear increase in temperature as air flows from one side to the other. The ventilation ducts enhance air movement, effectively promoting heat dissipation. The air temperature increases by 47.46 %, equivalent to 11.68 °C. Additionally, the cross-sectional cloud map confirms the heat exchange effect of the ventilation ducts. The presence of rectangular high-temperature zones is attributed to the high thermal conductivity of the partition wall in contact with the expanded clay aggregate above the gravel bedding. Ventilation ducts effectively remove heat to maintain stable foundation temperatures.

The external insulation layer of the storage tank effectively reduces heat loss. As shown in Fig. 11, the variation in heat flux distribution between the inner and outer layers is minimal, with most areas showing a difference of <3 W/m^2. This is due to the use of aluminum silicate, whose thermal conductivity is 0.08 W/m·°C, as a thermal insulator. The insulation layer significantly slows the heat transfer, resulting in a minimal temperature gradient between the inner and outer layers. It is noteworthy that within the cap 1 m of the tank, the increased thickness further reduces the temperature gradient between the inner and outer layers. However, at high liquid levels, the slight decrease in the tank temperature is also reflected in the variation in heat flux.

Fig. 12 illustrates the heat flux distribution across the base foundation layers of the storage tank, allowing for an assessment of whether the heat flux distribution is uniform and identifying potential hot or cold spots. The heat flux in the foundation layers decreases progressively from cap to bottom. However, because of the enhanced convective heat transfer from the air, the heat flux in the ventilation ducts increased to >38.6 W/m^2. As a result of the high thermal conductivity of the steel material, the regions with the highest heat flux are the ring support steel plate and the steel ring wall. The ring support steel plate helps to distribute the vertical load of the tank evenly across the other support structures of the foundation, thus partially mitigating localized stress concentration. However, as shown in the cloud plot, the ring support steel plate is in direct contact with the high-temperature tank side wall, leading to a thermal bridge effect at the junction with the lower edge of the tank side wall. The high thermal conductivity results in rapid heat transfer in the area above the steel plates, resulting in a high heat flux. The heat flux of the ring support steel plate for the hot tank reaches 1336.40 W/m^2, 2.34 times that of the cold tank. Additionally, the heat flux values are also notably high in the concrete partition wall, reaching 189.48 W/m^2. The partition wall is in contact with the expanded clay aggregate, which has good thermal insulation properties, resulting in lower temperatures at the bottom of the expanded clay aggregate. However, concrete has a significant thermal conductivity, exacerbating the temperature gradient between the two materials and increasing the heat flux. This trend is confirmed by the cloud plot in Fig. 12, which shows that the heat flux in the partition wall increases progressively from cap to bottom, consistent with the temperature gradient changes between the two materials.

As the primary insulating material in the base layer, the expanded clay aggregate shows its heat flux distribution recorded in Fig. 13. The cross-sectional heat flux distribution in the cloud plot exhibits minor, periodic fluctuations. Most of the heat flux at the upper areas are around 60 W/m^2, fluctuating within a range of 5 W/m^2, while the heat flux on the sides shows a significant increase, reaching up to 94.48 W/m^2. This increase is due to the contact between the upper surface of the expanded clay aggregate and the firebrick buttress as well as the fine gravel bedding, with the heat flux in the firebrick buttress being 1.45 times higher than that in the fine gravel bedding. The differences in heat flux between the two contact areas, particularly at the junction of these regions, are due to temperature gradients.

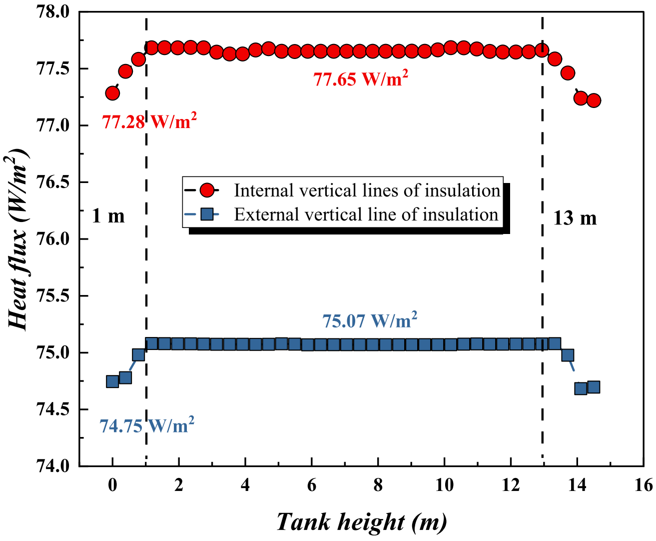

Fig. 11. Heat flux distribution in the vertical direction of the internal and external insulation.

Fig. 14 illustrates the calculation of heat loss from the storage tank and the temperature drop after 24 h, focusing primarily on the tank bottom, tank side wall, and tank cap. Thermal losses through the hot tank wall accounts for 49.21 % of the total heat loss, reaching 131.35 kW. This is primarily due to the large area of surface on the tank side wall, which is >1.69 times that of the tank bottom or tank cap. Comparing the heat flux distribution between the hot and cold tanks, the heat flux at the tank bottom and the tank cap shows minimal variation, while the heat flux through the tank side wall is consistently the highest, exceeding 75 W/m^2.

The storage tank is filled with 19,000 × 10^3 kg of MS, and the temperature of the hot and cold tank under full liquid level conditions decreased by 0.79 °C and 0.63 °C, respectively, after 24 h. These results are comparable to the temperature drop of 1 °C per day for a full tank reported by Relloso S [33]. The slightly lower temperature drop observed in this study is mainly due to the mass of salt in Relloso S's study being 285,000 × 10^3 kg, which is 1.5 times the amount used in this study. Additionally, the total heat loss reported by Relloso S is slightly lower than that of the hot tank in this study, with a difference of <20 W/m^2. This discrepancy may be attributed to the detailed modeling of the tank's foundation layers in this study, which could potentially overestimate the heat loss from the tank bottom.

4.2. Effect of different factors on the thermal performance of storage tanks

Analyzing the heat loss and temperature drop data can reveal potential shortcomings in the design. The effect of different parameters on the temperature field and heat loss is studied to determine the optimal configuration.

4.2.1. Environmental temperature

The change in ambient temperature affects various parts of the storage tank to different extents, with the insulation layer and some foundation materials being more significantly impacted. As shown in Fig. 15(a), the temperature change in the insulation layer is 55.74 °C, which falls within a moderate range. This is due to the large surface area of the insulation layer exposed to the external air, making it more susceptible to convective and conductive heat transfer effects. A reduction in convective effects might decrease the heat exchange rate of the insulation layer, while an increase in conductive effects could lead to more heat being transferred through the insulation layer to the external environment. Moreover, it is evident that as the depth of the foundation layer increases, the temperature fluctuations become more pronounced. This is because the lowest temperature is found in the underlying soil, leading to an increased temperature gradient. The maximum temperature difference reaches 89.09 °C, while the temperature variation in the expanded clay aggregate remains around 49.61 °C. The significant thickness and lower thermal conductivity of the expanded clay aggregate help mitigate most of the temperature gradient changes, resulting in relatively stable temperature fluctuations in the layers above it, which remain within a small range.

Fig. 15(b) compares the changes in heat flux, revealing that a decrease in ambient temperature leads to an increase in heat flux across various locations, primarily due to the overall increase in the system's temperature gradient. The cold tank's cap, being a region of significant heat loss, experiences a heat flux increase of 54.34 W/m^2. Notably, the heat flux of the ring support steel plate in the hot tank shows the most

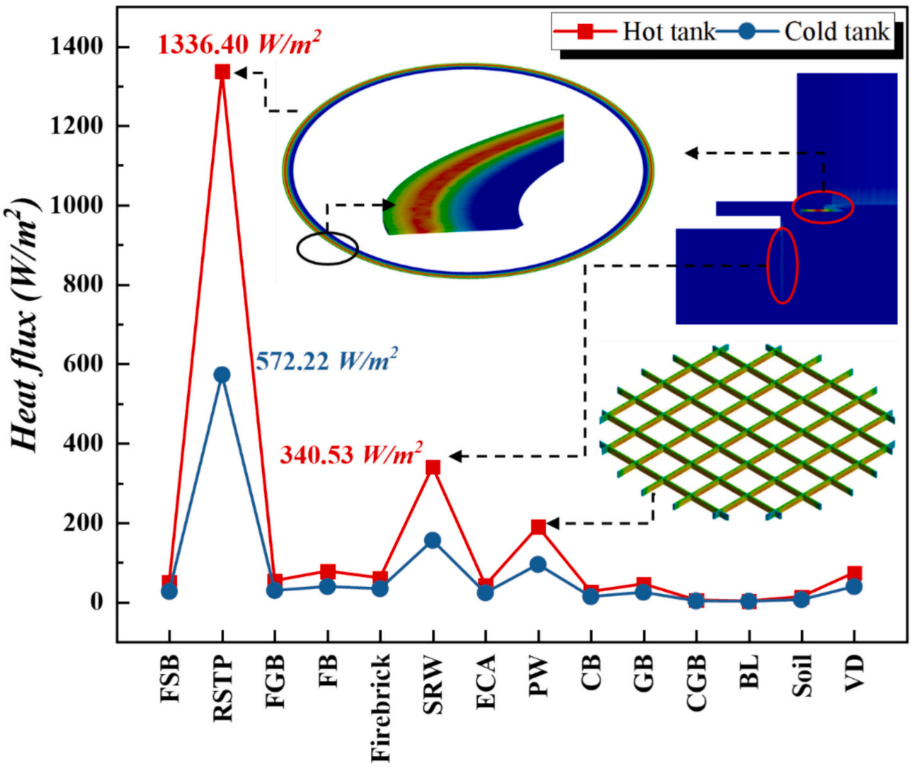

Fig. 12. Heat flux distribution in the foundation mat of the tanks.

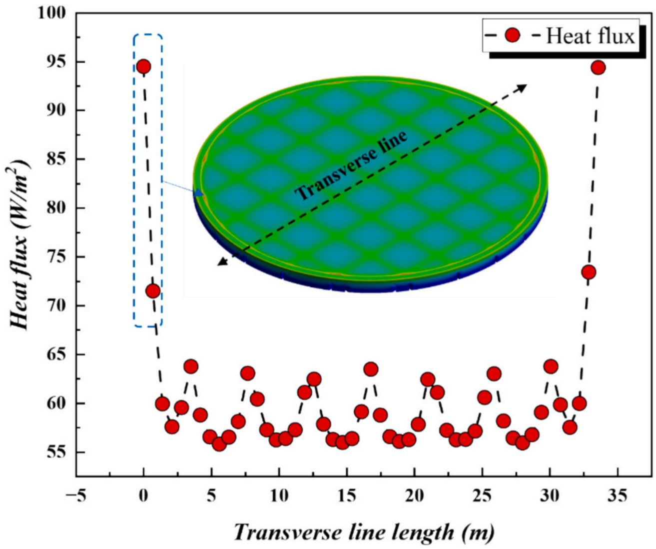

Fig. 13. Upper surface linear heat flux distribution of expanded clay aggregate.

significant change, reaching 1484.90 W/m^2, an increase of 17.65 %. The heat bridge effect created by the steel material is the primary reason for this excessive heat flux, consistent with the previous heat flux analysis.

Fig. 16 uses colored bars to illustrate the impact of ambient temperature on the heat loss of the storage tank, with gray bars representing the changes in temperature drop. The comparison reveals that total heat loss increases as the ambient temperature decreases, with the cold tank experiencing a rise of 32.58 %, equivalent to 60.65 kW. The heat loss from the tank side wall remains the largest, consistently accounting for over 49 % of the total heat loss. The primary contributors to heat dissipation are convection and radiation from the tank side wall surface to the environment. This loss is even more pronounced in the hot tank due to the increased radiation and convection losses at higher temperatures.

The temperature drop of both the hot and cold tanks after 24 h remains within 1 °C, even as the ambient temperature changes. Specifically, the temperature drop for the hot tank reaches 0.88 °C at −55 °C. In contrast, the temperature drops for the cold tank increases by 31.58 % as the ambient temperature decreases. The insulation thickness of the hot tank is 1.83 times that of the cold tank, primarily because it operates under high temperatures and requires thicker insulation to minimize heat loss and maintain its high-temperature state. On the other hand, the cold tank, which operates at lower temperatures, has a smaller temperature differential and lower heat loss requirement, allowing for thinner insulation. However, this also makes the cold tank more sensitive to changes in ambient temperature.

4.2.2. *Insulation thickness*

The variation in insulation thickness directly impacts the heat conduction efficiency of the MSST. Heat conduction occurs through energy transfer between molecules or atoms within a material. As shown in Fig. 17(a), the insulation layer exhibits the most significant temperature change, with the hot and cold tanks experiencing temperature changes of 17.15 °C and 19.92 °C, respectively. The change in insulation thickness primarily affects the tank's external heat loss but has a limited impact on maintaining the internal temperature of the tank and the foundation. Increasing the insulation thickness of the tank has minimal effect on the tank's internal temperature, resulting in negligible temperature fluctuations, which remain within 6.76 °C. The internal temperature of the tank is primarily governed by the balance between its heat source and heat loss.

The impact of insulation thickness on heat flux is primarily reflected in the inverse relationship described by the heat conduction equation. The primary function of the insulation layer is to reduce the temperature gradient, thereby decreasing heat flow. However, its effect on the internal temperature of the tank is relatively small, particularly when the insulation thickness has already reached a certain level, at which point

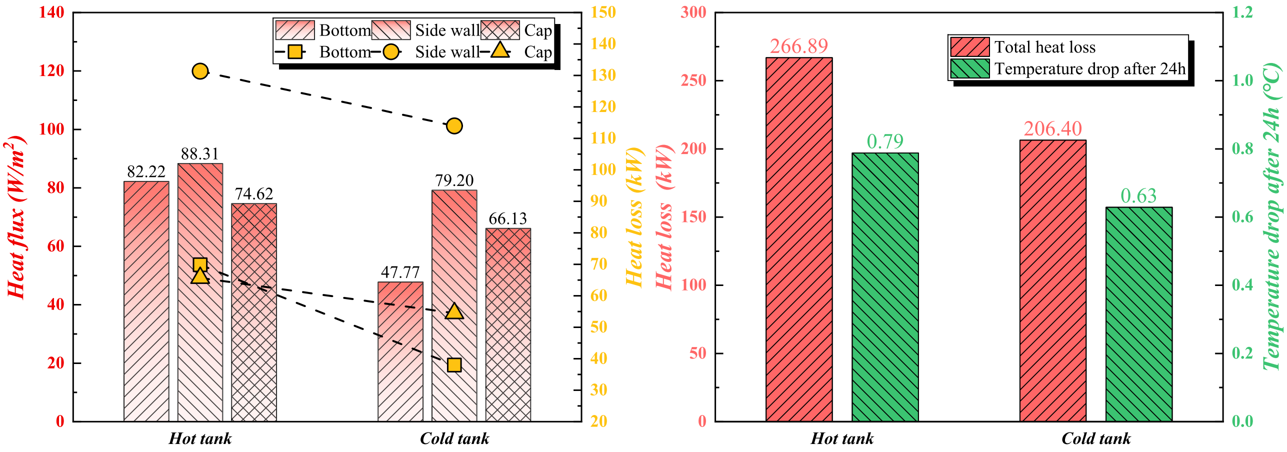

Fig. 14. Heat loss and temperature drop in tanks.

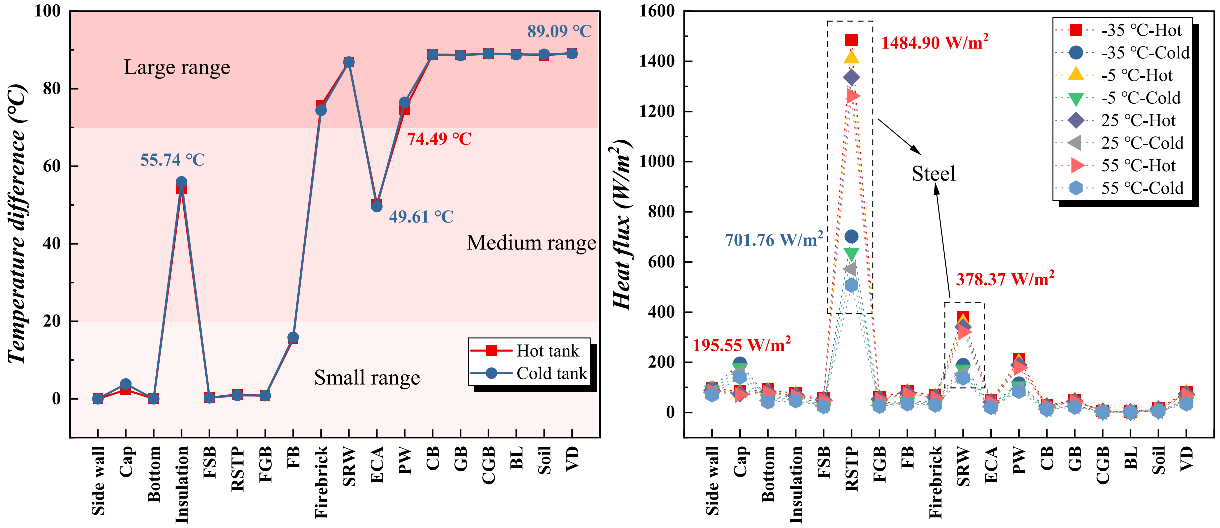

(a) Temperature difference (b) Heat flux

Fig. 15. Effect of ambient temperature on temperature and heat flux.

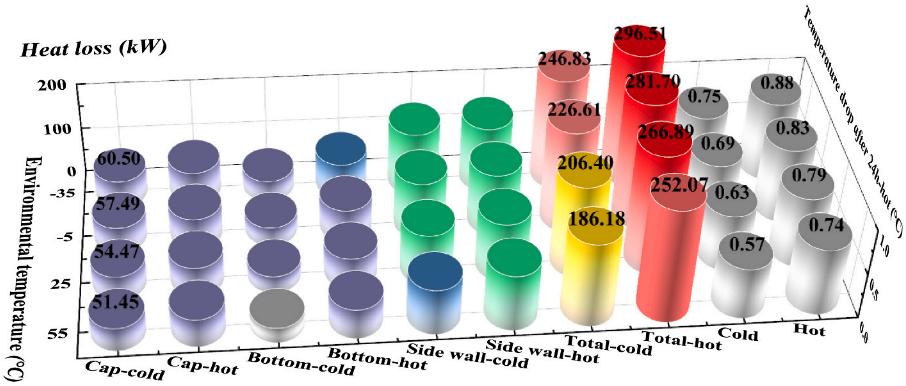

Fig. 16. Effect of ambient temperature on heat loss.

further increases in thickness yield diminishing returns. For instance, when the insulation thickness of the cold tank was increased from 300 mm to 400 mm, the heat flux decreased by only 1.3 W/m^2, which is just 0.95 % of the reduction achieved when increasing the thickness from 100 mm to 200 mm. The heat flux at various locations in the hot tank also showed a significant decrease, but the rate of decrease slowed down.

The insulation layer thickness is a critical factor in maintaining the

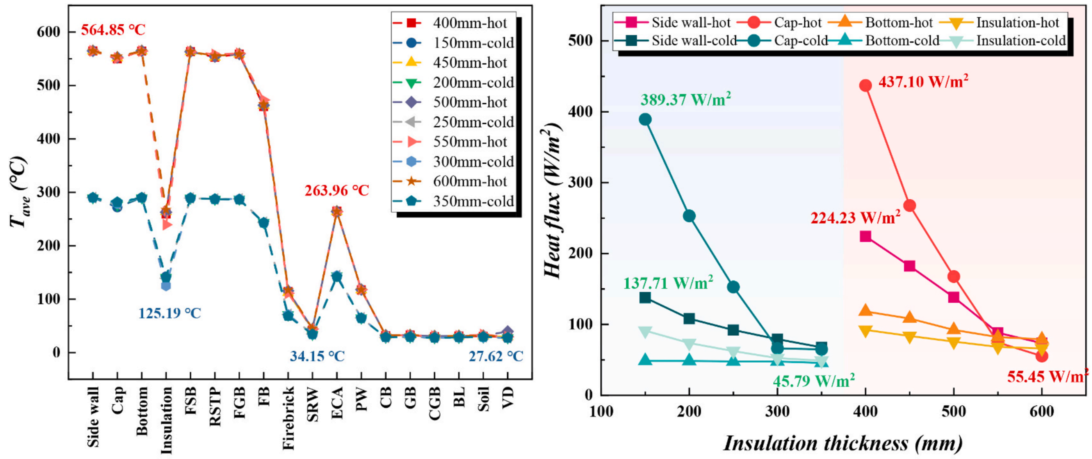

(a) Temperature (b) Heat flux

Fig. 17. Effect of insulation thickness on temperature.

temperature drop within 1 °C after 24 h. As illustrated in Fig. 18, the thermal loss and temperature drop were calculated, showing a similar trend to that observed with heat flux: the decrease in thermal loss gradually slows down. The thermal losses in the hot and cold tanks decreased by 74.45 % and 66.41 %, respectively. Notably, when the insulation thickness of the hot tank is reduced below 550 mm, the temperature drop exceeds 1 °C. Therefore, an insulation thickness of 300 mm to 550 mm for both the hot and cold tanks represents the optimal choice. In the design of insulation layers, increasing thickness generally means that materials with lower thermal conductivity can more effectively hinder heat transfer over a greater distance, thus reducing the heat flux through the insulation.

4.2.3. Expanded clay aggregate thickness

The thermal transfer path through the foundation is typically long, and the thermal conductivity of the foundation materials (such as concrete and gravel) determines how heat is conducted from the bottom of the storage tank to the foundation. Thermal conduction in the gravel bedding and expanded clay aggregate contributes to the internal temperature distribution, affecting how heat flows vertically and laterally across the base layer. High thermal conductivity in gravel bedding facilitates the rapid dissipation of heat across its volume, maintaining a relatively uniform temperature field when compared to materials with lower conductivity. However, expanded clay aggregate, often used for insulation due to its lower thermal conductivity, creates localized temperature gradients, thus acting as a thermal buffer to delay heat transfer to lower layers. As observed from the analyses in Fig. 6 and Fig. 7, expanded clay aggregate is the primary barrier to thermal transfer to the foundation. Fig. 19 examines the impact of expanded clay aggregate on the temperature of the foundation layer. With decreasing thickness of expanded clay aggregate in both the hot and cold tanks, there was an increase in the temperature difference in the diaphragm walls, up to 74.71 °C and 141.90 °C, respectively. Additionally, the temperature fluctuations in most of the foundation layers below the expanded clay aggregate rise by up to 30 °C, with a temperature difference of 24.4 °C observed in the firebricks of the hot tank. Notably, that the temperature of some foundation layers, particularly those above the expanded clay aggregate, such as the fine sand bedding, fine gravel bedding, and firebrick buttress, decreases as the expanded clay aggregate thickness is reduced. This is because, with reduced the expanded clay aggregate thickness, heat can diffuse more quickly through the fine gravel bedding. However, due to changes in heat flow, this results in a slight decrease in temperature.

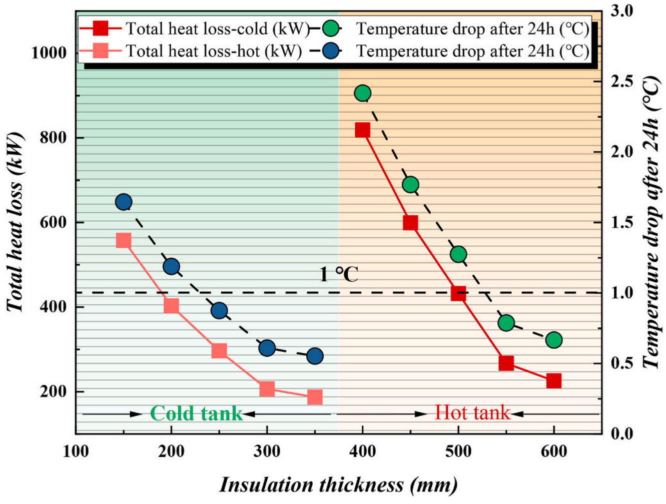

Fig. 18. Effect of insulation thickness on heat loss and temperature drop.

Thus, Fig. 20 discusses the heat flux and temperature drop data for the foundation layers on both sides of the expanded clay aggregate. The overall trend of heat flux for both hot and cold tanks is consistent; however, the reduction in expanded clay aggregate thickness has a more pronounced impact on the heat flux through the gravel bedding in the hot tank, reaching up to 116.89 W/m^2, compared to 56.99 W/m^2 in the cold tank. An increase in expanded clay aggregate thickness results in a decrease in both heat flux and temperature drop. This is because the increased thermal capacity of the entire foundation layer allows it to store more heat and release it more slowly. Consequently, the temperature drops for both the hot and cold tanks' expanded clay aggregate and the gravel bedding fall below 0.15 °C.

4.2.4. Ventilation

Foundation materials generally have a large thermal capacity, which results in slow temperature changes. However, when the foundation layer is subjected to thermal loads, excessive heat buildup can cause foundation materials to expand and contract thermally. This accumulated heat creates temperature gradients within the foundation layer, causing non-uniform expansion of the material and potentially leading to issues such as cracking and settling. To address these issues, ventilation ducts are typically installed at the bottom of the foundation to remove heat through convection, thereby keeping the foundation material below a critical temperature. The following discussion focuses on

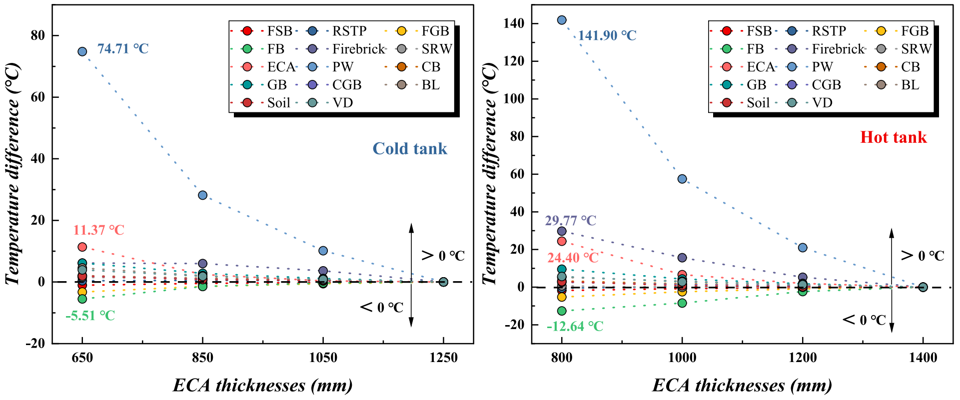

Fig. 19. Effect of expanded clay aggregate thickness on bedding temperature.

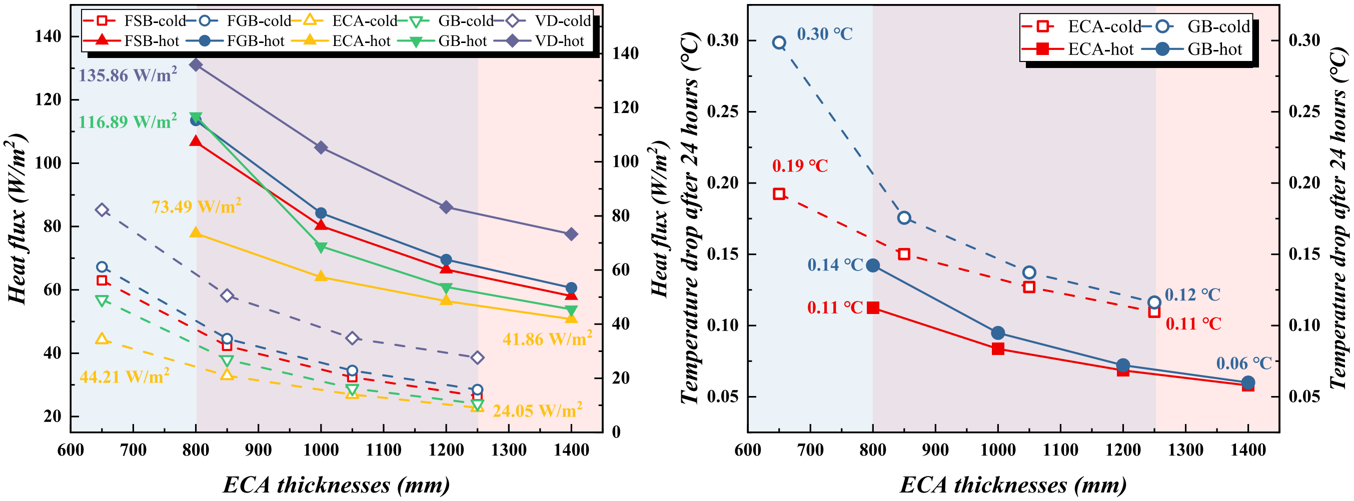

Fig. 20. Effect of expanded clay aggregate thickness on heat flux and temperature drop.

the impact of forced ventilation rate and the spacing of ventilation ducts on the temperature of the bottom layer of the foundation.

Fig. 21 reveals the distribution of heat flux from the ventilation ducts, indicating that the ventilation volume's impact is insignificant. For instance, the ventilation volume in the hot tank increased by 5.8 times, but the heat flux only rose by 4.79 %. This is because the temperature change between the interior and exterior of the ventilation duct is a key factor in determining the heat flux. The ventilation ducts are located below the expanded clay aggregate, with relatively stable temperatures. Although increasing ventilation volume enhances convective heat transfer, the efficiency of convective heat transfer is not perfectly linear. After a certain point, the effect of increasing ventilation volume on convective heat transfer diminishes. In contrast, the spacing of ventilation ducts directly affects the diffusion of heat within the foundation layer. For the hot tank, increasing the spacing of the ventilation ducts by 2.64 times resulted in a 1.97 times increase in heat flux. This is

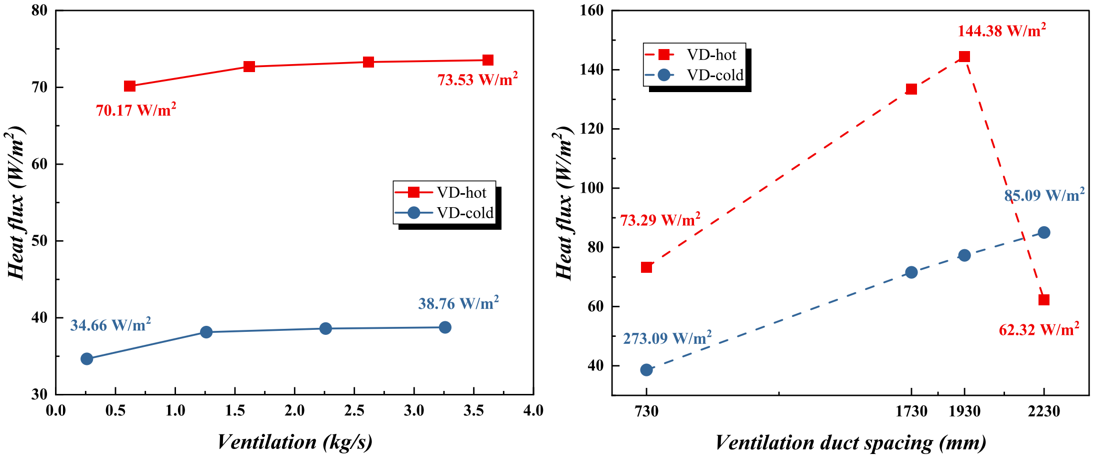

Fig. 21. Effects of ventilation on heat flux of ventilation ducts.

because larger spacing may cause heat accumulation within the foundation layer, reducing the effective transfer of heat to the ventilation ducts. It is noteworthy that when the spacing of the ventilation ducts in the hot tank exceeds 1930 mm, there is a sharp decrease in heat flux. This is because such spacing fails to meet the cooling demands of the foundation layer, leading to an overload on each ventilation duct and a sudden drop in the overall temperature gradient of the layer.

The analysis underscores that controlling the maximum temperature within the foundation layer is crucial for effective thermal management. Fig. 22 illustrates the impact of ventilation volume and spacing on the maximum temperatures of the foundation layer's upper and lower sides and the ventilation ducts. Clearly, increasing the ventilation volume significantly reduces the maximum temperature of the foundation layer. For both the hot and cold tanks, the highest temperature decreases by 26 %, although the rate of decrease diminishes over time. On the other hand, the spacing of ventilation ducts exhibits a typical linear correlation with the highest temperature. As the spacing increases, the maximum temperature in the upper layer of the cold tank rises by 16.86 °C. For the hot tank, a sharp increase in maximum temperature is observed, rising from 81.65 °C to 107.30 °C and reaching up to 260.00 °C, which confirms the influence of spacing on heat flux shown in Fig. 21. Therefore, while increasing the ventilation volume enhances the heat dissipation capacity of each ventilation duct, improper design of the ventilation duct spacing can result in inadequate heat removal despite increased airflow. This can lead to uncontrolled temperatures, as validated by the findings. Hence, considering the combined effects of ventilation volume and spacing is essential for improving ventilation efficiency and ensuring the foundation's safety.

5. Conclusion

This study evaluated the thermal performance of storage tanks in terms of heat loss and temperature drop. It was found through base case that the insulation layers effectively reduce temperature fluctuations on both the interior and exterior of the tanks. Expanded clay aggregate significantly mitigates heat transfer, resulting in a temperature gradient of 527.83 °C. Heat losses are measured at 266.89 kW for the hot tank and 206.40 kW for the cold tank, with temperature drops of 0.79 °C and 0.63 °C after 24 h, respectively.

The study also elucidated the effect of different factors on the thermal performance of the tanks. The main conclusions are as follows:

1. A decrease in ambient temperature significantly increases heat loss in the cold tank by 32.58 %, demonstrating a heightened sensitivity of the cold tank's temperature to ambient conditions.
2. A decrease in ambient temperature significantly increases heat loss in the cold tank by 32.58 %, demonstrating a heightened sensitivity of the cold tank's temperature to ambient conditions.
3. The thickness of the expanded clay aggregate is crucial in influencing heat transfer and temperature fluctuations. Reducing its thickness increases heat loss from the upper bedding while amplifying temperature gradients in the lower bedding, with maximum differences reaching 74.71 °C and 141.90 °C, respectively.
4. While ventilation flow has minimal impact on the heat flux of the bottom bedding, the spacing of ventilation ducts significantly affects heat dissipation. Excessive spacing can lead to heat accumulation, with critical limits identified at 1930 mm, beyond which heat flux and temperature control may be compromised.

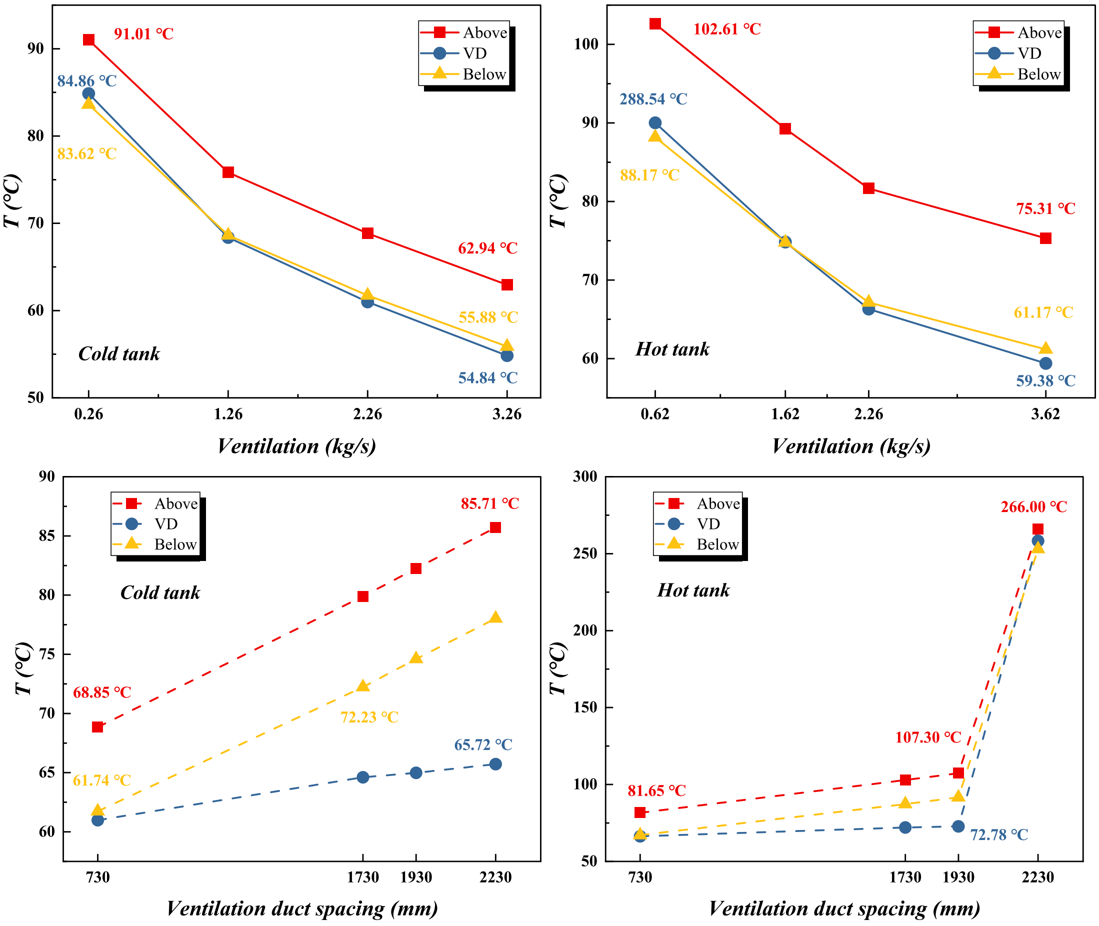

Fig. 22. Effect of ventilation on maximum temperatures in gravel bedding and ventilation ducts.

While this study offers valuable insights into the thermal behavior of molten salt storage tanks, the model can be improved for better accuracy and applicability. Incorporating advanced heat transfer mechanisms and considering changes in liquid level will enhance the understanding of heat loss. Including temperature-dependent material properties, such as thermal conductivity and thermal expansion coefficients, can provide realistic simulations of thermal stresses. Validating the model with field data from existing installations and focusing on the dynamic processes of charging and discharging molten salt will strengthen its practical relevance for solar power plant design and operation.

CRediT authorship contribution statement

Xue Xue: Writing – review & editing, Visualization, Supervision, Conceptualization. **Huaan Li:** Software, Methodology. **Cunxian Chen:** Software, Methodology. **Fengyongkang Wu:** Software, Methodology. **Kelang Jin:** Software, Methodology. **Mengting Ji:** Software, Methodology. **Hao Zhou:** Project administration, Investigation, Funding acquisition, Formal analysis.

Declaration of competing interest

The authors declare that they have no known competing financial interests or personal relationships that could have appeared to influence the work reported in this paper.

Acknowledgement

This work was supported by the Fundamental Research Funds for the Central Universities (2022ZFJH04).

Data availability

Data will be made available on request.

References

[1] IRENA, Renewable energy source – solar, Available from: http://wwwirenaorg/solar, 2018.

[2] T. Bauer, C. Odenthal, A. Bonk, Molten salt storage for power generation, Chem. Ing. Tech. 93 (2021) 534–546.

[3] Q. Yu, P. Fu, Y. Yang, J. Qiao, Z. Wang, Q. Zhang, Modeling and parametric study of molten salt receiver of concentrating solar power tower plant, Energy 200 (2020) 117505.

[4] Q. Yong, Y. Tian, X. Qian, X. Li, Retrofitting coal-fired power plants for grid energy storage by coupling with thermal energy storage, Appl. Therm. Eng. 215 (2022) 119048.

[5] M. Khani, M. Samiei Moghaddam, T. Noori, R. Ebrahimi, Integrated energy management for enhanced grid flexibility: optimizing renewable resources and energy storage systems across transmission and distribution networks, Heliyon 10 (2024) e39585.

[6] K. Jiang, Q. Wang, H. Liu, Q. Zhang, Z. Mu, Y. Niu, Dynamic simulation and control strategy development of molten salt steam generation system for coal-fired power plant flexible retrofit, Case Studies in Thermal Engineering 63 (2024) 105212.

[7] T. Ma, Z. Li, K. Lv, D. Chang, W. Hu, Y. Zou, Design and performance analysis of deep peak shaving scheme for thermal power units based on high-temperature molten salt heat storage system, Energy 288 (2024) 129557.

[8] K. Jiang, G. Zhang, H. Liu, Z. Mu, Q. Wang, T. Qin, et al., Design and dynamic simulation of flue gas-molten salt heat exchanger in flexible operation coal-fired power plant, Journal of Energy Storage 93 (2024) 112227.

[9] M. Mubarrat, M.M. Mashfy, T. Farhan, M.M. Ehsan, Research advancement and potential prospects of thermal energy storage in concentrated solar power application, Int. J. Thermofluids 20 (2023) 100431.

[10] U. Pelay, L. Luo, Y. Fan, D. Stitou, M. Rood, Thermal energy storage systems for concentrated solar power plants, Renew. Sustain. Energy Rev. 79 (2017) 82–100.

[11] L. Seyitini, B. Belgasim, C.C. Enweremadu, Solid state sensible heat storage technology for industrial applications – a review, J. Energy Storage 62 (2023) 106919.

[12] D.S. Jayathunga, H.P. Karunathilake, M. Narayana, S. Witharana, Phase change material (PCM) candidates for latent heat thermal energy storage (LHTES) in concentrated solar power (CSP) based thermal applications - a review, Renew. Sustain. Energy Rev. 189 (2024) 113904.

[13] C. Prieto, A. López-Román, L.F. Cabeza, Failure analysis of the leakage and ignition of heat transfer fluid in a concentrating solar power (CSP) pilot plant, Renew. Energy 237 (2024) 121554.

[14] K.E. N'Tsoukpoe, H. Liu, N. Le Pierrès, L. Luo, A review on long-term sorption solar energy storage, Renew. Sustain. Energy Rev. 13 (2009) 2385–2396.

[15] X. Py, N. Sadiki, R. Olives, V. Goetz, Q. Falcoz, Thermal energy storage for CSP (concentrating solar power), EPJ Web Conf (2017) 148.

[16] Concentrating solar power (CSP) projects. https://solarpaces.nrel.gov/ (Accessed on July 16, 2020).

[17] American Petroleum Institute (API) 650 Standard Welded Tanks for Oil Storage, 12th edition, American Petroleum Institute, Washington, 2013.

[18] J.M. Andújar, F. Rosa, M. Geyer, CESA-1 thermal storage system evaluation, Solar Energy 46 (1991) 305–312.

[19] M. Castro, J.L. Presa, J. Díaz, J. Peire, A.F. Baker, S.E. Faas, et al., C.R.S. Receiver and storage systems evaluation, Solar Energy 47 (1991) 197–207.

[20] L.G. Radosevich, C.E. Wyman, Thermal energy storage development for solar electrical power and process heat applications, Journal of Solar Energy Engineering 105 (1983) 111–118.

[21] X. Zhang, Y. Wu, C. Zhang, Temperature distribution and strength analysis of large-scale molten salt thermal storage tank, Journal of Beijing University of Technology 47 (2021) 1064–1073.

[22] B.-C. Du, Y.-F. Guo, C. Xu, L.-J. Huang, X.-F. Li, Y.-G. Lei, Dynamic creep and stress performances of the packed-bed thermal energy storage tank with molten salt EPCM particles, Appl. Therm. Eng. 225 (2023) 120247.

[23] Y.-F. Guo, B.-C. Du, C. Xu, Y.-G. Lei, Effects of EPCM particle properties on creep damage of the molten salt packed-bed thermal energy storage system, Journal of Energy Storage 68 (2023) 107808.

[24] Z. Tang, W.-Q. Tao, Strength analysis of molten salt tanks for concentrating solar power plants, Energy Storage and Saving 2 (4) (2023) 571–577.

[25] M. Laporte-Azcué, A. Acosta-Iborra, D. Santana, Estimation of solar receiver corrosion conditions during operation to aid in the design of receiver-corrosion lab tests, Sol. Energy Mater. Sol. Cells 266 (2024) 112701.

[26] Z. Wan, J. Wei, M.A. Qaisrani, J. Fang, N. Tu, Evaluation on thermal and mechanical performance of the hot tank in the two-tank molten salt heat storage system, Appl. Therm. Eng. 167 (2020) 114775.

[27] CSPPLAZA, Molten salt storage tanks at GemaSolar photovoltaic plant being rebuilt due to damage [EB/OL], Solar thermal power generation network (2017). https://www.cspplaza.com/article-9047-1.html, 2018.

[28] M.S. Mehos, H. Price, R. Cable, D.W. Kearney, B.D. Kelly, G.J. Kolb, et al., Concentrating Solar Power Best Practices Study, 2020.

[29] I. Rodríguez, C.D. Pérez-Segarra, O. Lehmkuhl, A. Oliva, Modular object-oriented methodology for the resolution of molten salt storage tanks for CSP plants, Appl. Energy 109 (2013) 402–414.

[30] C. Suárez, A. Iranzo, F.J. Pino, J. Guerra, Transient analysis of the cooling process of molten salt thermal storage tanks due to standby heat loss, Appl. Energy 142 (2015) 56–65.

[31] G. Peiró, J. Gasia, L. Miró, C. Prieto, L.F. Cabeza, Experimental analysis of charging and discharging processes, with parallel and counter flow arrangements, in a molten salts high temperature pilot plant scale setup, Appl. Energy 178 (2016) 394–403.

[32] C. Prieto, R. Osuna, A.I. Fernández, L.F. Cabeza, Thermal storage in a MW scale. Molten salt solar thermal pilot facility: plant description and commissioning experiences, Renew. Energy 99 (2016) 852–866.

[33] S. Relloso, E. Delgado, Experience with molten salt thermal storage in a commercial parabolic trough plant; Andasol 1 commissioning and operation, 2009, 14–8.

[34] J. Schulte-Fischedick, R. Tamme, U. Herrmann, CFD Analysis of the Cool Down Behaviour of Molten Salt Thermal Storage Systems, 2008.

[35] F. Zaversky, J. García-Barberena, M. Sánchez, D. Astrain, Transient molten salt two-tank thermal storage modeling for CSP performance simulations, Sol. Energy 93 (2013) 294–311.

[36] C. Prieto, R. Osuna, A.I. Fernández, L.F. Cabeza, Molten salt facilities, lessons learnt at pilot plant scale to guarantee commercial plants; heat losses evaluation and correction, Renew. Energy 94 (2016) 175–185.

[37] H. Zhou, H. Shi, Y.F. Zhu, W.F. Fang, An experimental investigation of temperature distribution and heat loss in molten salt tanks in concentrating solar power plants, JOURNAL OF RENEWABLE AND SUSTAINABLE ENERGY (2020) 12.

[38] H. Zhou, H. Shi, J.K. Zhang, M.X. Zhou, Experimental and numerical investigation of temperature distribution and heat loss of molten salt tank foundation at different scales, Heat Mass Transf. 56 (2020) 2859–2869.

[39] GB/T 700–2006 Carbon structural steel. Standardization Administration of the People's Republic of China, 2006.

[40] GB/T 16400–2003 Aluminum silicate cotton and its products for heat insulation. Standardization Administration of the People's Republic of China, 2003.

[41] GB 50017-2020 Standard for the Design of Steel Structures. Standardization Administration of the People's Republic of China, 2020.

[42] GB 50007-2011 Building Foundation Design Code. Standardization Administration of the People's Republic of China, 2020.

[43] Scientific ZJOo, Reports TIT. Solar Power Tower Design Basis Document, Revision, 2001.

[44] K.A. Khazaei, A.A. Hamidi, M. Rahimi, Numerical investigation of fuel dilution effects on the performance of the conventional and the highly preheated and diluted air combustion furnaces, Chin. J. Chem. Eng. 17 (2009) 711–726.

[45] S. Tsan-Hsing, W.L. William, S. Aamir, A new k-ε eddy viscosity model for high Reynolds number turbulent flows: model development and validation, Computers Fluids (1995) 24.

[46] E. Ebrahimnia-Bajestan, M. Khatibi, D. Wood, S.R. Maadi, Coupled thermal-optical numerical modeling of PV/T module – combining CFD approach and two-band radiation DO model, Energy Conversion Management 198 (2019) 111781.

[47] S. Yang, W. Tao, Heat Transfer, Fourth edition, Higher Education Press, 2006.

[48] R.W. Bradshaw, D.B. Dawson, W. De La Rosa, R. Gilbert, S.H. Goods, M.J. Hale, et al., Final Test and Evaluation Results from the Solar Two Project. United States, 2002.